Title: Retinal Calcium Waves Coordinate Uniform Tissue Patterning of the *Drosophila* Eye.

Authors: Ben Jiwon Choi*, Yen-Chung Chen, and Claude Desplan**

Affiliations:

Department of Biology, New York University, New York, NY 10003, USA

*Corresponding author. Email: b.jiwon.choi@gmail.com

** Corresponding author. Email: cd38@nyu.edu

Abstract: Optimal neural processing relies on precise tissue patterning across diverse cell types. Here, we show that spontaneous calcium waves arise among non-neuronal support cells in the developing *Drosophila* eye to drive retinal morphogenesis. Waves are initiated by Cad96Ca receptor tyrosine kinase signaling, triggering PLCγ-mediated calcium release from the endoplasmic reticulum. A cell-type-specific 'Innexin-code' coordinates wave propagation through a defined gap junction network among non-neuronal retinal cells, excluding photoreceptors. Wave intensity scales with ommatidial size, triggering stronger Myosin II-driven apical contractions at interommatidial boundaries in larger ommatidia. This size-dependent mechanism compensates for early boundary irregularities, ensuring uniform ommatidial packing critical for precise optical architecture. Our findings reveal how synchronized calcium signaling among non-neuronal cells orchestrates tissue patterning in the developing nervous system.

Main Text:

INTRODUCTION

Precise tissue patterning is crucial for the optimal functioning of biological systems (*1-3*). Sensory systems exemplify this principle with their arrangement of functional modules that is essential for processing sensory input (*4, 5*). To establish the functional organization of sensory modules, the overall architecture of the organ, mainly composed of non-neuronal cells including glial and epithelial cells, must be precisely patterned and coordinated with sensory neurons (*6-8*). However, despite its importance, patterning of non-neuronal components in sensory tissues is less understood than patterning of neuronal circuits.

Synchronized calcium activity in neuronal cells during development is crucial for the patterning of neuronal circuits (*9-12*). In the mammalian visual system, retinal waves are essential for the proper wiring of visual pathways, not just within the retina but also in higher brain areas (*13, 14*). While this calcium activity is also important for the development of surrounding non-neuronal cells, such as Müller glia or retinal pigment epithelium, its significance in instructing and coordinating architectural organization of the nervous system is still not well understood (*15-17*). Beyond the nervous system, synchronized calcium activity is known to be critical for the morphogenesis of various other tissues (*18-21*). For instance, calcium activity regulates the formation of skeletal muscle by coordinating the differentiation and fusion of myoblasts (*22*). Therefore, synchronized calcium activity might also have a significant developmental role in the structural patterning of non-neuronal cells in the nervous system.

In contrast to synaptic transmission-mediated synchronized calcium activity between neurons, intercellular calcium activity in non-neuronal cells is primarily mediated by gap junction channels (*18-20*). These channels form multicellular networks across diverse cell types, allowing them to synchronize their activities— a process essential for neural circuit development (*23, 24*). Beyond their role in nervous system development, gap junction networks are crucial for various biological processes, including tissue regeneration, cancer metastasis, and aging (*25-27*). However, technical difficulties have hindered a comprehensive understanding of their roles. These challenges include the complexity of live-cell imaging needed to track network activity and the difficulty of specifically manipulating gap junction channels, given their subunit diversity and vital role in cellular physiology (*23, 28*).

The *Drosophila* retina offers an excellent system for investigating the role of intercellular calcium activity among non-neuronal cells that could be important for its structural patterning (*29-31*). Its simplicity, combined with its stereotypic organization and genetic accessibility, allow for precise observation and manipulation of cellular processes through live imaging of intact specimens. It has recently been used to identify the role of calcium waves during late retinal development (*32*). The retina is composed of around 800 unit-eyes (ommatidia); each ommatidium houses eight photoreceptor neurons (**PRs**) (*33, 34*). These units are surrounded by specialized non-neuronal retinal support cells that exhibit features of glial and epithelial cells (**Fig. 2A, B**) (*35, 36*). They include four cone cells (**CC**), two primary pigment cells (**1PCs**), and a cluster of twelve inter-ommatidial cells (**IOCs**) that are shared among six adjacent ommatidia (*34, 36*). These IOCs include six secondary pigment cells (**2PCs**), three tertiary pigment cells (**3PCs**), and three bristle cells (**BCs**).

Both neuronal and non-neuronal cells in the retina are regionally patterned. For example, the dorsal rim area has specialized photoreceptor neurons for polarized light detection (*33*) while the dorsal third of the eye contains R7 color photoreceptors that co-express two UV-sensitive opsins (*37*). The ventral retina features structurally larger ommatidia compared to the dorsal side (*38, 39*). This regional patterning is evolutionarily conserved across fly species and

is linked to optimized visual behavior of ground features (*38*). The optic lobe circuitry also exhibits regional polarity, with distinct synaptic densities and neuronal subtypes between the dorsal and ventral sides (*40, 41*). These findings suggest that the fly visual system has robust regional patterning of both neuronal and non-neuronal populations that is crucial for the processing of visual information (*42*).

In this study, we optimized a versatile imaging platform to monitor calcium dynamics throughout the pupal stages of the intact *Drosophila* retina. We identified robust early retinal waves of synchronized calcium activity in retinal support cells just prior to synaptogenesis of photoreceptors to their optic lobe targets. We investigated the molecular mechanisms and developmental significance of these waves. Calcium release from the endoplasmic reticulum via IP_3 receptor is initiated by the receptor tyrosine kinase Cad96Ca and phospholipase Cγ. It propagates to adjacent cells through gap junctions, with unique Innexin subunit combinations involved in distinct cell types. Retinal waves drive calcium-dependent apical contraction of inter-ommatidial boundaries through IOC morphogenesis via the Myosin II pathway. Wave activity is more frequent in the ventral region of the eye, where larger ommatidia generate stronger calcium signals that promote more robust contractions. This mechanism compensates for initial boundary irregularities, ensuring uniform inter-ommatidial boundaries across the retina, which is critical for establishing consistent lens architecture. Therefore, we reveal the molecular and cellular mechanisms by which synchronized calcium activity in retinal support cells coordinate the overall architecture of the eye.

RESULTS

Early retinal calcium waves in the developing retina.

To explore pupal retinal development in *Drosophila*, we utilized a dry lens imaging platform to monitor calcium dynamics in the developing retina of intact animals **(Fig. 1A**). Compared to the immersion-lens protocol (*43, 44*), this approach provides notable advantages by eliminating the need for coverslips, enabling simpler and contact-free imaging of intact animals **(Fig. 1A, S1A**). Using this platform, we monitored calcium dynamics in the developing retina from its initial detachment from the cuticle (around 10 hours after pupal formation, 10hAPF) until eclosion (~100hAPF) **(Fig. 1B, S1A, Movie S1**). We expressed the genetically encoded calcium indicator GCaMP6s in all retinal cells using longGMR-GAL4 or GMR-GAL4 (Detailed in protocol) (*45, 46*). During our observations, two specific developmental windows displayed robust synchronized calcium activity across the whole retina **(Fig. 1B, S1A).** Early retinal waves, hereto referred to as "**retinal waves",** emerged at around 37hAPF and were sustained for roughly 3 hours **(Fig. 1B, S1A, Movie S1H)**. Later-stage calcium waves were observed starting from around 73hAPF and continued until eclosion **(Fig. 1B, S1A, Movie S1I**). These waves were previously described and analyzed (*32*).

We focused our observations on the early retinal waves with fine temporal resolution to determine their overall properties and function **(Fig. 1C-F, Movie S2**). During early pupal development before the onset of retinal waves, isolated calcium transients were only rarely observed in photoreceptor neurons (**PRs**) alone **(Fig. S1A2' arrow**). Retinal waves began as calcium signals in a single retinal cone cell (**CC**), first appearing at 37.1 ± 0.91 hAPF (SD, n=19), initiating what we define as early stage 1 **(Fig. 1C1 arrow, Movie S2A,** Detailed in **Fig. 2**). The signals then spread to adjacent cells within the same ommatidium during late stage 1 **(Fig. 1C2 arrowhead, Movie S2B**). These stage 1 waves lasted for 22±4.4 minutes **(Fig. 1D, F**). Then, the waves started spreading to adjacent ommatidia, which marked the onset of stage 2 **(Fig. 1C3, Movie S2C**). This phase was characterized by intense retinal calcium activity that persisted for 156±14 minutes **(Fig. 1D, F**). Subsequently, at 39.1 ± 0.86 hAPF, waves became

again restricted to a single ommatidium for 46 ±15 minutes (stage 3) **(Fig. 1C4, D-F, Movie S2D**). Later, most calcium activity faded, leaving sporadic calcium transients, mainly in PRs, which continued until the onset of the late retinal waves at 73.4 ± 1.26 hAPF (SD, n=7) **(Fig. S1A4', A9'**) (*32*). A detailed description of these wave patterns at single-cell resolution is provided in the next section. Both onset and duration of each stage of retinal waves were remarkably consistent between animals **(Fig. 1D-F**), occurring irrespective of the genetic drivers, calcium sensors, and excitation laser used **(Fig. S1C-E**). When we simultaneously imaged both eyes, the difference in the onset of the waves between eyes was only 2.4±1.7 minutes (SD, n=5), suggesting that the initiation of retinal waves is a bilaterally synchronized phenomenon **(Fig. S1B, Movie S3**).

We examined regional patterns of retinal waves by quantifying the amount of synchronized calcium activity occurring across multiple cells within each ommatidium. The ommatidial-level calcium activity first emerged in isolated ommatidia during late stage 1, predominantly in the ventral-anterior (**VA**) region **(Fig. 1G2, G3**). As the waves progressed to stage 2, they spread across neighboring ommatidia to encompass other retinal regions **(Fig. 1G4, G5**). To analyze wave activity across the population, we integrated data from multiple retinas by pooling them into an 8x8 grid template **(Fig. 1H**). This spatial analysis over the entire wave period revealed a distinct regional pattern, with increased wave activity in the VA region **(Fig. 1H, I**). This indicates that retinal waves have a distinct spatiotemporal pattern.

Single cell resolution of retinal waves reveals stereotypical patterns of initiation and propagation.

To examine retinal wave initiation and propagation at the single-cell level, we used Multi Color Flp-Out (**MCFO**)-based labeling at 40hAPF to map the spatial configuration of individual retinal cells **(Fig. 2A, B**) (*47*). Within a single ommatidium, all retinal cell types are in direct contact with each other **(Fig. 2A2', A3', B**), consistent with electron microscopy studies (*34*), providing a structural basis for single-cell tracing of retinal waves.

To determine the pathway through which retinal waves propagate, we performed high-resolution calcium imaging to detect single-cell calcium activity **(Fig. 2C, Movie S4**). Initial calcium activity began from single CCs **(Fig. 2C1 arrow, 2D1, D1'**), which then propagated to neighboring cells in a stereotypic manner **(Fig. 2D**). During Stage 1, the waves began in one CC, spread to adjacent CCs (**CC>CC, Fig. 2D2, D2'**), then moved to 1PCs (**CC>1PC, Fig. 2D3, D3'**) before reaching IOCs (**1PC>IOCs, Fig.2D4, D4'**), thus propagating within a single ommatidium (**CC>CC>1PC>IOCs**) **(Fig. 2D, E,** detailed in **S2A-D, Movie S5**). Calcium was thus released in all non-neuronal cell-types within a single ommatidium without ever involving PRs. These stereotypic wave propagation patterns progressed from the apical to the basal layer **(Fig. 2D**), defining **CC>CC>1PC>IOCs** as a **'vertical pathway**' (**Fig. 2H**). Importantly, although all retinal cells within a single ommatidium are in physical contact **(Fig. A2', A3'**), we did not observe alternate wave propagation routes, such as from 1PC to CC**,** CC to IOCs bypassing 1PC, or IOCs to 1PC.

The defining feature of Stage 2 is the lateral spread of calcium activity to neighboring ommatidia. These inter-ommatidial waves were mediated by IOCs, following the completion of the vertical activation pathway **(Fig. 2C3, F, G**). Two adjacent ommatidia always share IOCs, allowing an activated IOC in one ommatidium (**O1**) to directly contact CCs and other IOCs in the neighboring ommatidium (**O2**) **(Fig. 2F, G**). During wave propagation from O1 to O2 **(Fig. 2F, G**), the calcium signal spread from this initial IOC (e.g., 2PC labeled '**1'**) to adjacent CCs (e.g., '**2**') and IOCs (e.g., '**3**' and '**4**') through basal layer connections **(Fig. 2G2**). Consequently, these inter-ommatidial waves (**IOC > CC** and **IOC > IOCs**) spread laterally

across the basal layers of multiple ommatidia, forming a **'lateral pathway' (Fig. 2G, H,** detailed in **S2E, Movie S6**). The lateral propagation moved across successive ommatidia, with IOC > IOCs propagation forming the leading edge of the wave. Meanwhile, activated CCs along the wave's path initiated their own vertical pathways within each ommatidium, activating the remaining cells. This coordinated mechanism ultimately enabled the activation of all retinal support cells along the wave's trajectory, establishing robust, reliable, and region-specific calcium signaling **(Fig. 2H**).

Both vertical and lateral waves then stopped with only minimal, sporadic calcium activity in both CC and 1PCs that defined stage 3 **(Fig. 2C4, Movie S4D**). Since we never observed significant calcium activity or propagation to PRs, we looked for any potential involvement of PRs. GCaMP6s driven by a PR-specific GAL4 driver (Chaoptin-GAL4) did not reveal any significant calcium activity in PRs during the waves **(Fig. S3A, Movie S7**) showing that retinal waves are entirely driven by non-neuronal retinal cells, similarly to what was observed for late retinal waves (*32*).

In summary, although all retinal cells within a single ommatidium are physically interconnected, retinal waves do not randomly diffuse across neighboring cells. Rather, the waves show a highly organized pattern: They exclusively initiate in CC, then propagate along stereotypic vertical and then lateral pathways **(Fig. 2H**), suggesting an underlying dedicated cellular communication network.

Cad96Ca-PLCγ-IP$_3$R signaling triggers calcium release from the ER

The waves we observe in non-neuronal cells in the *Drosophila* retina resemble the calcium waves seen in glia and epithelial cells in vertebrate neurodevelopment (*20*). In mammals, the endoplasmic reticulum (**ER**) serves as the primary source of these intercellular calcium waves (*20, 48*), suggesting a similar role in *Drosophila* retinal waves. To simultaneously measure calcium levels in both the ER and the cytoplasm, we used two calcium indicators with different colors: ER-targeted GCaMP (green), and cytosolic jRgeco1a (red) **(Fig. 3A, Movie S8**) (*49-51*). During waves, when calcium levels increased in the cytoplasm of a cell, they decreased in the ER across all retinal supporting cells **(Fig. 3A, B**), indicating active calcium release from the ER.

To identify the molecular mechanisms involving calcium release from the ER, we analyzed the contribution of the inositol trisphosphate receptor (**IP$_3$R**), a crucial component of calcium wave dynamics across various models (*48*). We generated retinal mosaic mutants using an ey-Flpase **(Fig. 3C**), where wild-type (**WT**) tissue was marked with RFP, and *IP$_3$R* mutant clones (**Mut**) were not labeled **(Fig. 3C1**) (*32, 52*). In mosaic eyes, retinal waves neither initiated nor spread in *IP$_3$R* mutant clones **(Fig. 3C2, Movie S9**), resulting in significantly reduced calcium activity in these cells **(Fig. 3D**). This suggests that IP$_3$R-mediated ER calcium release is cell-autonomously required for initiating and propagating retinal waves.

To address the mechanisms that activate IP$_3$R-dependent calcium release during the retinal waves, we investigated the role of the Phospholipase C (**PLC**) pathway that generates inositol trisphosphate (**IP$_3$**) from phosphatidylinositol 4,5-bisphosphate (PiP$_2$) (*53*). Among the five PLCs in the fly genome, only PLCβ (encoded by ***norpA***) and PLCγ (encoded by ***sl***) are expressed in the retina (*54, 55*). Retinas of *norpA* null mutants exhibited normal wave activity, but no waves were observed in *sl* null mutants **(Fig. 3E2, E3, F, Movie S10C**), indicating that PLCγ plays a critical role in generating calcium activity during the waves. Although *sl* null mutants are viable, they show developmental defects, including impaired retinal growth **(Fig. S3C2, D**) (*55*). To selectively inhibit PLCγ in the mid-pupal retina, we used longGMR-Cas9 to generate *sl*-targeting somatic CRISPR knockout (**sKO**) retinas (*56*), bypassing early retinal

development. The resulting *sl*-sKO mutant retinas exhibited only slightly reduced growth **(Fig. S3C, D**) but showed a 90% wave activity reduction, consistent with *sl* null mutants **(Fig. 3E4, F, Movie S10D**), and thus confirming the specific role of PLCγ in initiating retinal waves.

Receptor tyrosine kinases (**RTK**s) are upstream regulators of PLCγ signaling (*57*). To determine the pathway that activates PLCγ, we screened fifteen potential RTKs based on their expression patterns in the developing retina (*58*). We examined how retinal waves were affected by inhibiting these RTKs using somatic CRISPR, RNAi, or dominant negative transgenes (**Table S1**). Our candidate screening showed that only *cad96Ca* was necessary for retinal waves initiation without altering gross retinal morphology **(Fig. 3E5, F, S3C4, D, Table S1**). *cad96Ca* (also called *stit*) is an RTK with a cadherin-like domain that is involved in epidermal wound healing (*59, 60*), but its role in retinal development is not known. We examined *cad96Ca* expression in the retina. Live snapshots of retinas with nuclear-localized GFP driven by *cad96Ca*-GAL4 showed expression in all types of retinal support cells, including CCs, but not in PRs **(Fig. S3E, F**), consistent with a role for Cad96Ca in initiating retinal waves. Overall, these results suggest that Cad96Ca acts upstream of the PLCγ-IP_3R pathway, inducing ER-release calcium activity in CCs during the initiation of retinal waves.

Retinal waves propagate through gap-junctions mediated by cell-specific combinations of Innexins.

The crucial role of gap-junction signaling in driving propagation of intercellular calcium waves is well-documented across different biological systems, including the mammalian retina (*20, 61, 62*). In *Drosophila*, the eight members of the *innexin* (***inx***) gene family encode gap-junction subunits that assemble into octameric hemi-channels forming gap junction channels at cell junctions (*63-65*). All *innexin* genes, except *inx4* and *inx5*, are expressed in the retina (*65, 66*). To analyze their precise distribution, we performed retinal immunostainings for all eight Innexin subtypes. In 40hAPF retinas, Inx1 (encoded by *ogre*), Inx2 and Inx3 were observed at the junctions of non-neuronal retinal cells **(Fig. 4A, B, S4A**) (*65-67*). They were localized in puncta that represent gap-junction plaques (**GJP**) adjacent to the junctional marker Disc large1 (**Dlg1**) **(Fig. 4A1, S4A**) (*68, 69*). Super-resolution STED imaging confirmed that Inx2 and Inx3 strictly coincided with GJP **(Fig. 4A2', S4A**) while Inx1 that was primarily localized within GJPs was also observed outside **(Fig. 4B1'**). In contrast, we did not detect Inx4, 5, 6, 7, or 8 in retinal cell junctions **(Fig. S4B**). Inx8 (also called *shakB*) was only detected in synapses within the optic lobe at 48hAPF, after the waves **(Fig. S4B, C**) (*65, 66*). Retinal waves remained unchanged in *inx8* mutants **(Fig. S4D, E, Movie S11**). Given that Inx2 and 3 GJPs were absent in PR somas within the retina **(Fig. S4A4', A5'**), these data suggest that neither Inx8 nor PRs play a role in propagating retinal waves.

To selectively inhibit *innexin* expression in at the mid-pupal retina, we used somatic CRISPR knockouts (**sKO**) using longGMR-Cas9. Immunostaining confirmed the near-complete loss of sKO-targeted *innexins* **(Fig. 4B2', B3'', B4''', S4-I**) in 40hAPF retinas. While sKO of *inx-1, -2, or -3* did not alter the onset of retinal waves or spontaneous activity in individual CCs **(Fig. 4F, S4J**), each uniquely affected stereotypic steps in wave propagation **(Fig. 4C, G, S4J, Movie S12**):

- *inx2*-sKO exhibited a drastic disruption of the propagations of all waves **(Fig. 4C3, D-G, S4J**).
- In contrast, *inx*1-sKO retinas only exhibited a slight decrease of the vertical and lateral wave pathways (**Fig. 4C2, D-G, S4J**).
- *Inx3*-sKO retinas maintained the initial vertical propagation from CC to 1PCs, but the propagation from 1PCs to IOCs was severely disrupted (**Fig. 4C4, D, G, S4J**), resulting in a

substantial reduction in the lateral pathway (**Fig. 4E**). In these *inx3*-sKOs, we also observed reverse propagation from 1PC to CC (**1PC>CC**) **(Fig. 4D**), which was never observed in wild type retinas.

- Since both inx1 and *inx3*-sKOs showed partial wave disruptions (**Fig. 4C-G**), we examined double somatic knockout of *inx1* and *inx3* (***inx1+3*-DsKO**) **(Fig. 4B5, C5**). In these *inx1+3*-DsKO retinas, every aspect of wave propagation was disrupted to a similar extent as seen in *inx2*-sKO (**Fig. 4C5, D-F**).
- We also detected altered spontaneous calcium activity within individual cells between 37hAPF and 40hAPF in *inx2, inx3,* and *inx1+3*-DsKO retinas. While these *innexin* mutations resulted in no or only a slight decrease in spontaneous firing in CCs, infrequent ectopic individual firing was also observed in retinal cell types such as 1PCs and IOCs (**Fig. 4F, S4J**). This suggests that innexins may act to suppress ectopic firing in non-CC cells.

To elucidate the distinct roles of each Innexin, we focused on the formation of gap junction plaques (**GJPs**) **(Fig. 4A, B**) that are critical for organizing gap-junction channels (*68, 70*). Inx2 is important for the localization of Inx1 and Inx3 to cell junctions in the developing retina (*67*). Consistently, we found that GJPs disappeared in *inx2*-sKO retinas, leading to dispersed staining of Inx1 and Inx3 outside of cell-junctions (**Fig. 4B3', B3'', S4G, I**). In *inx1*-sKO retinas, GJPs were still present but were slightly reduced in size, as observed with Inx2 and 3 immunostaining (**Fig. 4B2'', B2''', S4H, I**). In contrast, GJPs disappeared in IOCs in *inx3*-sKO retinas, while smaller GJPs remained in other cell types (**Fig. 4B4', B4'', S4G, H**). In *inx1+3*-DsKO retinas, the GJPs were absent at all cell junctions, similar to *inx2*-sKO (**Fig. 4B5, S4G-I**). As expected, whenever GJPs disappeared upon knock-out of a given *innexin*, the non-targeted Innexins were still detectable but were dispersed outside of cell-junctions **(Fig. 4B3', B3''', B5''**). These data indicate that each cell type has a specific set of Innexins contributing to GJPs.

In summary, our study highlights the unique roles of Innexins in regulating retinal wave activity through the formation of gap junction plaques. While all retinal support cells have GJPs containing Inxs1-3, Inx2 is essential for GJP assembly in all cell types, whereas Inx3 is specifically required in IOCs. Inx1 has a minor impact on its own but appears to compensate for the absence of Inx3 in CCs and 1PCs. When GJPs were disrupted, the corresponding wave propagation pathway was also disrupted **(Fig. 4G**), illustrating the importance of precise Innexin combinations in plaques for directing waves across distinct retinal cell types.

Retinal waves regulate Myosin II-driven apical remodeling that scales with ommatidial size.

Retinal waves generate spatially patterned calcium signals with a distinct ventral-anterior bias **(Fig. 5A1, 1I**). We identified a regional distribution of ommatidial size, with larger ommatidia also in the ventral-anterior region **(Fig. 5A1'**) at 36hAPF, just prior to the onset of the waves. This spatial pattern correlated with the distribution of retinal wave activity **(Fig. 5B**) - *i.e.* these larger ommatidia exhibited stronger retinal wave activity. To understand how this differential wave activity potentially influences the development of ommatidia in this region, we compared ommatidia before and after the wave period **(Fig. 5C, D**). Prior to the waves, larger ommatidia exhibited wider inter-ommatidial gaps formed by apical domain of IOCs **(Fig. 5C1, C1', D, E**): The 20% largest ommatidia from the ventral-anterior had wider boundaries than the 20% smallest from the dorsal-posterior **(Fig. 5F**). After the waves, inter-ommatidial gaps significantly contracted throughout the retina (**Fig. 5D, E**), while ommatidial size slightly increased (**Fig. S5B**). Importantly, larger ommatidia with initially wider gaps exhibited stronger boundary contraction (**Fig. 5E, F**). As a result, inter-ommatidial boundaries

became uniformly narrow across the retina (**Fig. 5C2, C2', F**), despite persistent regional variability in ommatidial size (**Fig. S5A2**). MCFO-based single-cell labeling confirmed that this contraction resulted from apical morphogenesis of IOCs (**Fig. S5C-E**).

To assess whether retinal waves were required for this size-dependent contraction of ommatidial boundaries, we analyzed mutants with severely disrupted retinal wave activity, either across all retinal cells (***sl*-sKO**) or specifically in IOCs (***inx3*-sKO**) (**Fig. 5A2, A3, B**). Before retinal waves, ommatidial size distribution and boundary morphology were similar to control in both mutants (**Fig. 5A2', A3'**). However, after retinal waves, boundary contraction failed in both mutants, resulting in ommatidial boundaries that remained immature and wider, independent of ommatidial size (**Fig. 5C3, C4, G, Detailed in S5F**), suggesting that retinal waves are essential for ommatidial boundary contraction. The similar phenotypes observed in *inx3*-sKO and *sl*-sKO mutants (**Fig. 5G**) highlight the critical role of IOCs in driving ommatidial boundary maturation.

To further test how retinal waves coordinate boundary contraction in relation to ommatidial size, we analyzed *inx1*-sKO mutants, which exhibit uniformly low calcium activity across all ommatidia, uncoupling calcium signaling from ommatidial size (**Fig. 5A4, B**). As a result, boundary contraction failed selectively in the larger ventral-anterior ommatidia, while smaller ommatidia still showed proper contraction (**Fig. 5C5, C5', G, S5F**). This suggests that wider initial boundaries require proportionally stronger wave activity to achieve uniform boundary maturation.

To directly test whether retinal waves drive apical boundary contraction proportionally to their activity level, we manipulated calcium levels using the heat-activated calcium channel TrpA1 (*71, 72*). In *sl*-sKO mutants, which lack endogenous retinal waves, weak heat induction of TrpA1 (15 min) during the endogenous wave time period (37hAPF) only rescued boundary contraction in smaller ommatidia, while larger ommatidia failed to fully contract (**Fig. 5C6, C6', G, S5F**). In contrast, stronger calcium induction (40 min) rescued boundary contraction in larger ommatidia (**Fig. 5C7', G, S5F**) but caused abnormal contraction in smaller ommatidia, resulting in narrow and wrinkled boundaries (**Fig. 5C7**). These results support the hypothesis that the higher intensity of calcium signaling due to more frequent retinal waves drives stronger apical contraction and ensures uniform ommatidial organization.

To determine how retinal waves promote contraction of the apical domain of IOCs in proportion to calcium activity levels, we examined the non-muscle myosin II pathway. IP_3R-mediated calcium release activates myosin light chain kinase, which phosphorylates non-muscle myosin II to form an actomyosin network, promoting contractility (*73, 74*). To examine the activation of the Myosin II pathway in response to calcium, we performed time-lapse imaging of retinas expressing GFP-tagged Sqh (Myosin II regulatory light chain). We observed Sqh-GFP signal primarily on the apical side of the retina as puncta of varying sizes (**Fig. 5H, S5G**), indicating discrete actomyosin foci representing localized contractile activity (*75*). To quantify these dynamics, we calculated the coefficient of variation (**CV**) of Sqh-GFP intensity along inter-ommatidial boundaries (*76*). During retinal waves, Sqh-GFP CV progressively increased, indicating the formation of larger and more organized actomyosin clusters within the inter-ommatidial boundaries (**Fig. 5H1-5, I**). This network assembly is consistent with wave-driven apical contraction of IOCs. Notably, Sqh-GFP aggregation was more pronounced in IOCs from larger ommatidia compared to smaller ones (**Fig. 5H5, H5', I**), supporting our model that stronger local calcium signals generate greater contractile forces, essential for robust apical IOC contraction in larger ommatidia. Actomyosin network formation was significantly impaired in both *sl* and *inx3*-sKO mutants (**Fig. 5J2, J3, K**), while *inx1*-sKO mutants exhibited reduced Sqh-GFP clustering selectively in large ommatidia (**Fig. 5J4', K**). These findings

suggest that disrupted wave activity compromises boundary contraction and actomyosin network assembly, emphasizing the necessity of proper actomyosin network formation for precise ommatidial remodeling.

Altogether, these results reveal that retinal waves coordinate apical contraction by scaling actomyosin network assembly proportionally to ommatidial size and boundary width, ensuring effective boundary contraction for uniform retinal morphogenesis.

Retinal Wave Activity Ensures Eye Uniformity in Adults

To determine the functional significance of retinal waves, we investigated how disrupted retinal waves during the mid-pupal stage affect adult retinal architecture, specifically ommatidial boundary development. By 72 hAPF, the IOC apical domain establishes distinct ommatidial boundaries as IOCs extend basal lens footings at ommatidial edges (**Fig. 6A2**, red arrow), providing structural support for corneal lens (**Fig. 6A7**). These footings not only anchor corneal lenses but also support pseudocones, specialized extracellular structures positioned between the lens and photoreceptor neurons **(Fig. 6B**) (*77*). Together, corneal lenses and pseudocones ensure precise light transmission to photoreceptor neurons. The spatial organization of these structures was quantified in a single plane at the pseudocone layer (**Fig. 6C**).

In control retinas, pseudocone size correlated with ommatidial size: the dorsal-posterior (**DP**) region contained smaller pseudocones, while the ventral-anterior (**VA**) region had larger pseudocones **(Fig. 6D6, D6', E**). Despite regional differences in pseudocone size, consistently low variability within each region indicates locally uniform pseudocone organization **(Fig. 6F**). In contrast, *sl*-sKO mutants showed severely disrupted pseudocone organization, although the outer lens surface appeared mostly normal **(Fig. S3C**). Lens footings at 72 hAPF were defective as anticipated from earlier IOC defects (**Fig. 6A3, A3'**), resulting in irregular pseudocone arrangements in adult retinas **(Fig. 6D2, D7, D7'**). Pseudocone sizes increased slightly (**Fig. 6D7, E**), but their variability significantly increased in both DP and VA regions (**Fig. 6D7, D7', F**). These results show retinal waves are essential for uniformly structured pseudocones by properly maturing IOCs during mid-pupal development.

Mutants with varying retinal wave activity further supported this conclusion. In *inx1*-sKO mutants, lens footings and pseudocones remained normal in the DP region with small ommatidia, while variability greatly increased in the VA region (**Fig. 6D3, D8, D8', F**), consistent with defective IOC development where ommatidia are larger (**Fig. 5C5'**). TrpA rescue experiments in *sl*-sKO mutants revealed regional differences in restoration: Weak rescue (15-minute heat induction) selectively improved lens footing structure and pseudocone uniformity in the DP region but not in the VA region (**Fig. 6D4, D9, D9', F**). Strong rescue (40-minute heat induction) improved pseudocone uniformity in both DP and VA regions (**Fig. 6D10, D10', F**), although lens footings in the DP region remained defective (**Fig. 6D5, D10**), matching IOC defects seen in smaller ommatidia at 46hAPF (**Fig. 5C7**).

Overall, these results demonstrate that retinal waves coordinate calcium-driven apical morphogenesis in proportion to ommatidial size, ensuring uniform retinal architecture essential for precise visual function. This highlights how synchronized calcium signaling directs tissue patterning (**Fig. 6G**).

DISCUSSION

We described here the intricate dynamics of calcium activity due to retinal waves during early *Drosophila* retinal development and showed how it shapes retinal architecture by

controlling the maturation of interommatidial cells. This provides insight into how directed synchronized calcium activity orchestrates structural patterning in tissues.

Establishment of Architectural Tissue Patterning through Calcium Waves in Non-Neuronal Cells.

While synchronized calcium activity is crucial for neuronal connectivity, its role in nervous system tissue organization remains unclear. Non-neuronal support cells such as radial glial cells in the rodent cortex, show strong synchronized calcium activity in early development (*20*). However, previous studies primarily focused on their roles in cellular proliferation and differentiation, often treating them as a permissive phenomenon for neuronal development (*20*).

In insects, ommatidial size plays a crucial role in optimizing visual function. Larger ommatidia have larger lenses that enhance light capture and improve visual sensitivity, whereas smaller ommatidia increase resolution by capturing finer spatial details. This regional variation in ommatidial size is an evolutionarily conserved feature across fly species with ventral ommatidia detecting closer and larger ground features that are darker than sky landscapes (*38, 39*). Despite this regional heterogeneity in ommatidial size, we found that inter-ommatidial boundaries remain uniformly spaced across the *Drosophila* retina, which is essential for maintaining a smooth and regularly patterned optical surface, ensuring proper lens alignment in the adult eye. Retinal waves mediate compensatory interommatidial cell (IOC) maturation, ultimately normalizing inter-ommatidial spacing across the retina. Therefore, early synchronized calcium activity in non-neuronal support cells actively shapes tissue architecture.

Parallels between Calcium waves in the Vertebrate and Fly Retinas

In vertebrates, non-neuronal support cells like radial glia or retinal pigment epithelium (**RPE**) cells exhibit gap-junction-mediated intercellular calcium waves prior to synaptogenesis. The embryonic chick RPE cells resemble the fly's IOCs, supporting PRs and maintaining retinal structure (*78-80*). While RPE function is well-documented with respect to eye diseases, neurodegeneration, and aging in humans, the dynamics and role of RPE calcium waves remain underexplored.

As synapses form, synchronized neuronal activity, driven by neurotransmission, emerges throughout the nervous system and is crucial for circuit formation (*13, 14*). In flies, gap-junction-mediated calcium waves in retinal support cells occur before synaptogenesis. This is followed later in development by neurotransmission-dependent synchronized activity in PRs and higher-order neurons. This activity, known as patterned stimulus-independent neuronal activity (**PSINA**), is essential for synaptic connectivity (*61, 81, 82*) . These parallels in sequential occurrences of synchronized activity from non-neuronal cells to neurons suggest that *Drosophila* could be a valuable model for studying vertebrate calcium dynamics during development.

Triggering Mechanism of Retinal Waves

The early retinal waves we observed occur at a very precise stage, suggesting that they are a developmental process that must be synchronized with other developmental events. This activity is initiated via Cad96Ca-PLCγ-IP_3R-mediated calcium release from the ER, suggesting that an extrinsic signal activating the receptor tyrosine kinase Cad96Ca orchestrates the timing of retinal waves coordinated with other developmental events. Although the ligand for Cad96Ca remains unidentified, recent studies suggest that insect juvenile hormone can activate Cad96Ca in cotton bollworm (*83*). Juvenile hormone exhibits multiple peaks, including one at

the mid-pupal stage, which coincides with the onset of retinal waves (*84*). This raises the possibility that juvenile hormone, or a related signal, could control Cad96Ca pathway.

Early and Late Calcium Waves and Morphological Development:

The developing fly retina undergoes two distinct calcium wave dynamics: early and late retinal waves. The function of late waves (occurring from ~73hAPF) has been explored (*32*) based on the phenotype of *IP_3R* mutants that show defective basal floor meshwork with stress fibers failing to contract. These defective contractions persist into adulthood, resulting in aberrant retinal morphology and an impaired extracellular matrix. In our study, *PLCγ* or *inx*s mutants led to nearly identical basal floor meshwork defects at 72h APF, *i.e.* before the onset of late waves **(Fig. S5H, I**). Since IP_3R is necessary for both early and late waves, the defects seen in *IP_3R* mutants cannot be attributed solely to late waves. Although further studies are necessary, our findings suggest that early waves, along with late retinal waves, contribute to basal floor meshwork development.

Calcium signals activate the non-muscle myosin II pathway leading to contraction of IOCs.

Our findings indicate that retinal waves leading to calcium signaling are crucial in organizing retinal architecture by activating the non-muscle myosin II pathway in IOC. This represents a critical mechanism through which spatial signaling shapes cell morphology. As ectopic calcium signals via TrpA channels restored IOC contraction, this suggests that calcium has an instructive role in regulating cellular morphogenesis. It should be noted that retinal waves generate periodic signals whereas TrpA-induced activity is more sustained: Future studies using optogenetics and high-resolution calcium imaging will be essential to determine the role of calcium signals in tissue organization and morphogenesis (*71*).

Limitation of the study

This study has several limitations affecting the interpretation of retinal wave patterning. First, the lack of cell-type-specific manipulation limits comprehensive mapping of wave propagation pathways and gap-junction networks. Second, the underlying mechanisms generating regionally biased and size-matched wave activity remain unexplored. Third, the roles of photoreceptors or wrapping glia, which contact the retina but do not exhibit calcium activity during waves, require further investigation. Finally, downstream signaling beyond Myosin II remains insufficiently characterized. Addressing these limitations through advanced genetic tools and strategies would provide a more comprehensive understanding of retinal wave functions and their broader relevance beyond *Drosophila*.

References and Notes

1. Y. C. Chen, N. Konstantinides, Integration of Spatial and Temporal Patterning in the Invertebrate and Vertebrate Nervous System. *Front Neurosci* **16**, 854422 (2022).
2. E. Heller, E. Fuchs, Tissue patterning and cellular mechanics. *J Cell Biol* **211**, 219-231 (2015).
3. T. Lecuit, P. F. Lenne, Cell surface mechanics and the control of cell shape, tissue patterns and morphogenesis. *Nat Rev Mol Cell Biol* **8**, 633-644 (2007).
4. T. A. Seabrook, T. J. Burbridge, M. C. Crair, A. D. Huberman, Architecture, Function, and Assembly of the Mouse Visual System. *Annu Rev Neurosci* **40**, 499-538 (2017).
5. N. Uchida, C. Poo, R. Haddad, Coding and transformations in the olfactory system. *Annu Rev Neurosci* **37**, 363-385 (2014).
6. M. Takeichi, Dynamic contacts: rearranging adherens junctions to drive epithelial remodelling. *Nat Rev Mol Cell Biol* **15**, 397-410 (2014).
7. L. E. Clarke, B. A. Barres, Emerging roles of astrocytes in neural circuit development. *Nat Rev Neurosci* **14**, 311-321 (2013).
8. U. Tepass, The apical polarity protein network in Drosophila epithelial cells: regulation of polarity, junctions, morphogenesis, cell growth, and survival. *Annu Rev Cell Dev Biol* **28**, 655-685 (2012).
9. Y. Tezuka, K. M. Hagihara, K. Ohki, T. Hirano, Y. Tagawa, Developmental stage-specific spontaneous activity contributes to callosal axon projections. *Elife* **11**, (2022).
10. F. J. Martini, T. Guillamon-Vivancos, V. Moreno-Juan, M. Valdeolmillos, G. Lopez-Bendito, Spontaneous activity in developing thalamic and cortical sensory networks. *Neuron* **109**, 2519-2534 (2021).
11. R. A. Baines, M. Landgraf, Neural development: The role of spontaneous activity. *Curr Biol* **31**, R1513-R1515 (2021).
12. O. Akin, B. T. Bajar, M. F. Keles, M. A. Frye, S. L. Zipursky, Cell-type-Specific Patterned Stimulus-Independent Neuronal Activity in the Drosophila Visual System during Synapse Formation. *Neuron* **101**, 894-904 e895 (2019).
13. J. B. Ackman, M. C. Crair, in *Curr. Opin. Neurobiol.* (2014), vol. 24, pp. 166-175.
14. L. A. Kirkby, G. S. Sack, A. Firl, M. B. Feller, A role for correlated spontaneous activity in the assembly of neural circuits. *Neuron* **80**, 1129-1144 (2013).
15. J. M. Tworig, M. B. Feller, Muller Glia in Retinal Development: From Specification to Circuit Integration. *Front Neural Circuits* **15**, 815923 (2021).
16. A. Lakkaraju *et al.*, The cell biology of the retinal pigment epithelium. *Prog Retin Eye Res*, 100846 (2020).
17. M. Hoon, H. Okawa, L. Della Santina, R. O. Wong, Functional architecture of the retina: development and disease. *Prog Retin Eye Res* **42**, 44-84 (2014).
18. S. Paudel, R. Sindelar, M. Saha, Calcium Signaling in Vertebrate Development and Its Role in Disease. *Int J Mol Sci* **19**, (2018).
19. J. C. Herve, M. Derangeon, Gap-junction-mediated cell-to-cell communication. *Cell Tissue Res* **352**, 21-31 (2013).
20. L. Leybaert, M. J. Sanderson, in *Physiol. Rev.* (American Physiological Society, 2012), vol. 92, pp. 1359-1392.
21. G. Dupont, L. Combettes, L. Leybaert, Calcium dynamics: spatio-temporal organization from the subcellular to the organ level. *Int Rev Cytol* **261**, 193-245 (2007).
22. J. Chal, O. Pourquie, Making muscle: skeletal myogenesis in vivo and in vitro. *Development* **144**, 2104-2122 (2017).

23. M. J. Vaughn, J. S. Haas, On the Diverse Functions of Electrical Synapses. *Front Cell Neurosci* **16**, 910015 (2022).
24. A. Arjun McKinney, R. Petrova, G. Panagiotakos, Calcium and activity-dependent signaling in the developing cerebral cortex. *Development* **149**, dev198853. (2022).
25. M. J. Zeitz, J. W. Smyth, Gap Junctions and Ageing. *Subcell Biochem* **102**, 113-137 (2023).
26. T. Aasen, M. Mesnil, C. C. Naus, P. D. Lampe, D. W. Laird, Gap junctions and cancer: communicating for 50 years. *Nat Rev Cancer* **17**, 74 (2017).
27. P. Wong *et al.*, The Role of Connexins in Wound Healing and Repair: Novel Therapeutic Approaches. *Front Physiol* **7**, 596 (2016).
28. J. Stephan, S. Eitelmann, M. Zhou, Approaches to Study Gap Junctional Coupling. *Front Cell Neurosci* **15**, 640406 (2021).
29. J. Malin, C. Desplan, Neural specification, targeting, and circuit formation during visual system assembly. *Proc Natl Acad Sci U S A* **118**, (2021).
30. J. R. Sanes, S. L. Zipursky, Design principles of insect and vertebrate visual systems. *Neuron* **66**, 15-36 (2010).
31. H. J. Bellen, C. Tong, H. Tsuda, 100 years of Drosophila research and its impact on vertebrate neuroscience: a history lesson for the future. *Nat Rev Neurosci* **11**, 514-522 (2010).
32. D. F. Ready, H. C. Chang, Calcium waves facilitate and coordinate the contraction of endfeet actin stress fibers in Drosophila interommatidial cells. *Development* **148**, (2021).
33. M. F. Wernet, M. W. Perry, C. Desplan, The evolutionary diversity of insect retinal mosaics: common design principles and emerging molecular logic. *Trends Genet* **31**, 316-328 (2015).
34. R. L. Cagan, D. F. Ready, The emergence of order in the Drosophila pupal retina. *Dev Biol* **136**, 346-362 (1989).
35. M. A. Charlton-Perkins, M. Friedrich, T. A. Cook, Semper's cells in the insect compound eye: Insights into ocular form and function. *Dev Biol* **479**, 126-138 (2021).
36. J. E. Treisman, Retinal differentiation in Drosophila. *Wiley Interdiscip Rev Dev Biol* **2**, 545-557 (2013).
37. E. O. Mazzoni *et al.*, Iroquois complex genes induce co-expression of rhodopsins in Drosophila. *PLoS Biol* **6**, e97 (2008).
38. A. D. Buffry *et al.*, Evolution of compound eye morphology underlies differences in vision between closely related Drosophila species. *BMC Biol* **22**, 67 (2024).
39. N. Posnien *et al.*, Evolution of eye morphology and rhodopsin expression in the Drosophila melanogaster species subgroup. *PLoS One* **7**, e37346 (2012).
40. A. Nern *et al.*, Connectome-driven neural inventory of a complete visual system. *Nature*, (2025).
41. M. N. Ozel *et al.*, Neuronal diversity and convergence in a visual system developmental atlas. *Nature* **589**, 88-95 (2021).
42. F. Pichaud, F. Casares, Shaping an optical dome: The size and shape of the insect compound eye. *Semin Cell Dev Biol* **130**, 37-44 (2022).
43. O. Akin, S. L. Zipursky, Frazzled promotes growth cone attachment at the source of a Netrin gradient in the Drosophila visual system. *Elife* **5**, (2016).
44. M. Langen *et al.*, The Developmental Rules of Neural Superposition in Drosophila. *Cell* **162**, 120-133 (2015).

45. S. E. Escobedo, A. Shah, A. N. Easton, H. Hall, V. M. Weake, Characterizing a gene expression toolkit for eye- and photoreceptor-specific expression in Drosophila. *Fly (Austin)* **15**, 73-88 (2021).
46. T. W. Chen *et al.*, Ultrasensitive fluorescent proteins for imaging neuronal activity. *Nature* **499**, 295-300 (2013).
47. A. Nern, B. D. Pfeiffer, G. M. Rubin, Optimized tools for multicolor stochastic labeling reveal diverse stereotyped cell arrangements in the fly visual system. *Proc Natl Acad Sci U S A* **112**, E2967-2976 (2015).
48. P. Chakraborty, G. Hasan, ER-Ca(2+) stores and the regulation of store-operated Ca(2+) entry in neurons. *J Physiol* **602**, 1463-1474 (2024).
49. C. H. Liu *et al.*, Rapid Release of Ca(2+) from Endoplasmic Reticulum Mediated by Na(+)/Ca(2+) Exchange. *J Neurosci* **40**, 3152-3164 (2020).
50. J. de Juan-Sanz *et al.*, Axonal Endoplasmic Reticulum Ca(2+) Content Controls Release Probability in CNS Nerve Terminals. *Neuron* **93**, 867-881 e866 (2017).
51. H. Dana *et al.*, Sensitive red protein calcium indicators for imaging neural activity. *Elife* **5**, (2016).
52. K. Venkatesh, G. Hasan, Disruption of the IP3 receptor gene of Drosophila affects larval metamorphosis and ecdysone release. *Curr Biol* **7**, 500-509 (1997).
53. J. W. Putney, T. Tomita, Phospholipase C signaling and calcium influx. *Adv Biol Regul* **52**, 152-164 (2012).
54. S. S. Balakrishnan, U. Basu, P. Raghu, Phosphoinositide signalling in Drosophila. *Biochim Biophys Acta* **1851**, 770-784 (2015).
55. A. Schlesinger, A. Kiger, N. Perrimon, B. Z. Shilo, Small wing PLCgamma is required for ER retention of cleaved Spitz during eye development in Drosophila. *Dev Cell* **7**, 535-545 (2004).
56. F. Port, H. M. Chen, T. Lee, S. L. Bullock, Optimized CRISPR/Cas tools for efficient germline and somatic genome engineering in Drosophila. *Proc Natl Acad Sci U S A* **111**, E2967-2976 (2014).
57. K. Kanemaru, Y. Nakamura, Activation Mechanisms and Diverse Functions of Mammalian Phospholipase C. *Biomolecules* **13**, (2023).
58. M. A. Charlton-Perkins, E. D. Sendler, E. K. Buschbeck, T. A. Cook, Multifunctional glial support by Semper cells in the Drosophila retina. *PLoS Genet* **13**, e1006782 (2017).
59. S. Mele, T. K. Johnson, Receptor Tyrosine Kinases in Development: Insights from Drosophila. *Int J Mol Sci* **21**, (2019).
60. S. Wang *et al.*, The tyrosine kinase Stitcher activates Grainy head and epidermal wound healing in Drosophila. *Nat Cell Biol* **11**, 890-895 (2009).
61. B. J. Choi, Y. D. Chen, C. Desplan, Building a circuit through correlated spontaneous neuronal activity in the developing vertebrate and invertebrate visual systems. *Genes Dev* **35**, 677-691 (2021).
62. R. A. Pearson *et al.*, Ca(2+) signalling and gap junction coupling within and between pigment epithelium and neural retina in the developing chick. *Eur J Neurosci* **19**, 2435-2445 (2004).
63. J. Guiza, I. Barria, J. C. Saez, J. L. Vega, Innexins: Expression, Regulation, and Functions. *Front Physiol* **9**, 1414 (2018).
64. I. M. Skerrett, J. B. Williams, A structural and functional comparison of gap junction channels composed of connexins and innexins. *Dev Neurobiol* **77**, 522-547 (2017).
65. L. A. Stebbings *et al.*, Gap junctions in Drosophila: developmental expression of the entire innexin gene family. *Mech Dev* **113**, 197-205 (2002).

66. G. Ammer, R. M. Vieira, S. Fendl, A. Borst, Anatomical distribution and functional roles of electrical synapses in Drosophila. *Curr Biol* **32**, 2022-2036 e2024 (2022).
67. M. Richard, R. Bauer, G. Tavosanis, M. Hoch, The gap junction protein Innexin3 is required for eye disc growth in Drosophila. *Dev Biol* **425**, 191-207 (2017).
68. S. McCutcheon, R. F. Stout, Jr., D. C. Spray, The dynamic Nexus: gap junctions control protein localization and mobility in distinct and surprising ways. *Sci Rep* **10**, 17011 (2020).
69. S. Roberts, C. Delury, E. Marsh, The PDZ protein discs-large (DLG): the 'Jekyll and Hyde' of the epithelial polarity proteins. *FEBS J* **279**, 3549-3558 (2012).
70. D. Segretain, M. M. Falk, Regulation of connexin biosynthesis, assembly, gap junction formation, and removal. *Biochim Biophys Acta* **1662**, 3-21 (2004).
71. T. Honda, Optogenetic and thermogenetic manipulation of defined neural circuits and behaviors in Drosophila. *Learn Mem* **29**, 100-109 (2022).
72. S. R. Pulver, S. L. Pashkovski, N. J. Hornstein, P. A. Garrity, L. C. Griffith, Temporal dynamics of neuronal activation by Channelrhodopsin-2 and TRPA1 determine behavioral output in Drosophila larvae. *J Neurophysiol* **101**, 3075-3088 (2009).
73. J. Wang, M. Michel, L. Bialas, G. Pierini, C. Dahmann, Preferential recruitment and stabilization of Myosin II at compartment boundaries in Drosophila. *J Cell Sci* **136**, (2023).
74. M. A. Quintanilla, J. A. Hammer, J. R. Beach, Non-muscle myosin 2 at a glance. *J Cell Sci* **136**, (2023).
75. M. R. Stachowiak *et al.*, Self-organization of myosin II in reconstituted actomyosin bundles. *Biophys J* **103**, 1265-1274 (2012).
76. P. Zhao *et al.*, Aurora-A Breaks Symmetry in Contractile Actomyosin Networks Independently of Its Role in Centrosome Maturation. *Dev Cell* **49**, 651-653 (2019).
77. M. Charlton-Perkins, N. L. Brown, T. A. Cook, The lens in focus: a comparison of lens development in Drosophila and vertebrates. *Mol Genet Genomics* **286**, 189-213 (2011).
78. S. Yang, J. Zhou, D. Li, Functions and Diseases of the Retinal Pigment Epithelium. *Front Pharmacol* **12**, 727870 (2021).
79. I. S. Tarau, A. Berlin, C. A. Curcio, T. Ach, The Cytoskeleton of the Retinal Pigment Epithelium: from Normal Aging to Age-Related Macular Degeneration. *Int J Mol Sci* **20**, (2019).
80. R. A. Pearson, N. Dale, E. Llaudet, P. Mobbs, ATP released via gap junction hemichannels from the pigment epithelium regulates neural retinal progenitor proliferation. *Neuron* **46**, 731-744 (2005).
81. B. T. Bajar *et al.*, A discrete neuronal population coordinates brain-wide developmental activity. *Nature* **602**, 639-646 (2022).
82. O. Akin, S. L. Zipursky, Activity regulates brain development in the fly. *Curr Opin Genet Dev* **65**, 8-13 (2020).
83. C. Aa *et al.*, Peripartum severe acute maternal morbidity in low-risk women: A population-based study. *Midwifery* **119**, 103602 (2023).
84. J. L. Scanlan, C. Robin, C. K. Mirth, Rethinking the ecdysteroid source during Drosophila pupal-adult development. *Insect Biochem Mol Biol* **152**, 103891 (2023).

ACKNOWLEDGMENTS
We thank the members of the Desplan lab for helpful discussions and manuscript feedback; J. Malin, S. Cordoba, and D. Chen for advice on manuscript preparation; N. Ghosh and J. Treisman for technical assistance with cryosectioning; M. Hoch and A. Borst for antibodies; P. Phelan for *shakB²* fly stocks; and M. Courgeon for plasmids. We used stocks obtained from the Bloomington Drosophila Stock Center (NIH P40OD018537). This work also benefited from antibodies and *Drosophila* lines generated with support from the CGSB at NYU Abu Dhabi.

Funding:
This work was supported by NIH grants EY13010 and EY017916 (C.D.), NIH fellowship F32EY027682 (B.J.C.), the MacCracken Fellowship at New York University (Y.-C.C.), a NYSTEM institutional training grant (C322560GG) (Y.-C.C.), and a scholarship to study abroad from the Ministry of Education, Taiwan (Y.-C.C.).

Author contributions:
B.J.C. and C.D. conceived the project, analyzed the data, and wrote the manuscript. Y.-C.C. performed quantitative analysis of calcium imaging data. B.J.C. performed all experiments.

Competing interests:
The authors declare no competing interests.

Data and materials availability:
All data are available from the lead contacts, Claude Desplan (cd38@nyu.edu) and Ben Jiwon Choi (B.Jiwon.Choi@gmail.com). Antibodies and fly lines will be distributed upon request.

Use of AI technologies:
During the preparation of this work, the authors used ChatGPT Plus to improve readability. After using this tool, the authors reviewed and edited the content as needed and take full responsibility for the content of the publication.

Supplementary Materials

Materials and Methods

Figs. S1 to S5

Tables S1 to S3

References (*85,86*)

Movies S1 to S12

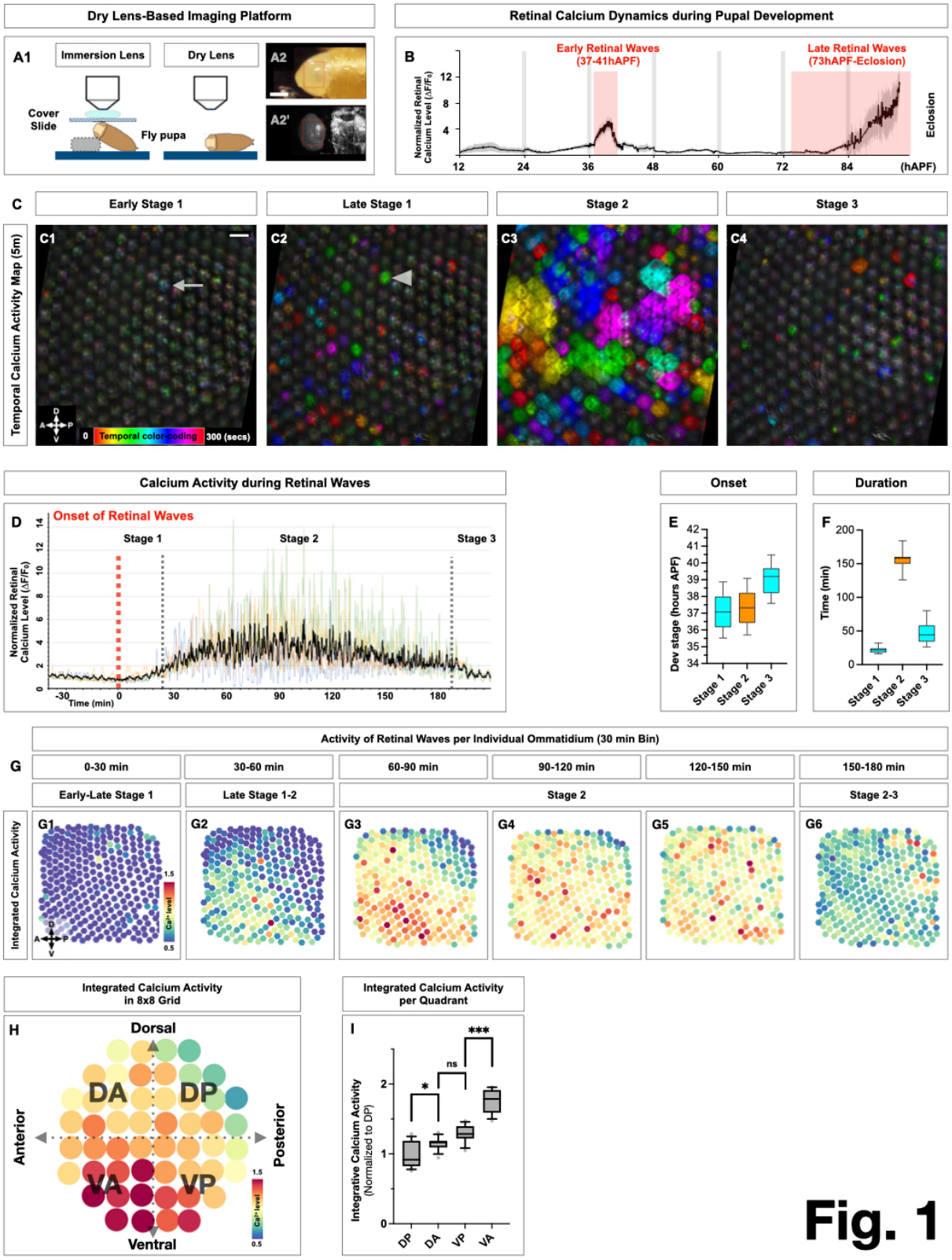
Dry Lens-Based Imaging Platform
A1
Immersion Lens
Dry Lens
Cover Slide
Fly pupa
A2
A2'
Retinal Calcium Dynamics during Pupal Development
B
Early Retinal Waves (37-41hAPF)
Late Retinal Waves (73hAPF-Eclosion)
Normalized Retinal Calcium Level (ΔF/F₀)
Eclosion
(hAPF)
C
Early Stage 1
Late Stage 1
Stage 2
Stage 3
Temporal Calcium Activity Map (5m)
C1
C2
C3
C4
Temporal color-coding
300 (secs)
Calcium Activity during Retinal Waves
D
Onset of Retinal Waves
Stage 1
Stage 2
Stage 3
Time (min)
Onset
Duration
E
Dev stage (hours APF)
F
Time (min)
Activity of Retinal Waves per Individual Ommatidium (30 min Bin)
G
0-30 min
30-60 min
60-90 min
90-120 min
120-150 min
150-180 min
Early-Late Stage 1
Late Stage 1-2
Stage 2
Stage 2-3
Integrated Calcium Activity
G1
G2
G3
G4
G5
G6
Integrated Calcium Activity in 8x8 Grid
H
Dorsal
Ventral
Anterior
Posterior
DA
DP
VA
VP
Integrated Calcium Activity per Quadrant
I
Integrative Calcium Activity (Normalized to DP)
ns
DP
DA
VP
VA

Fig. 1

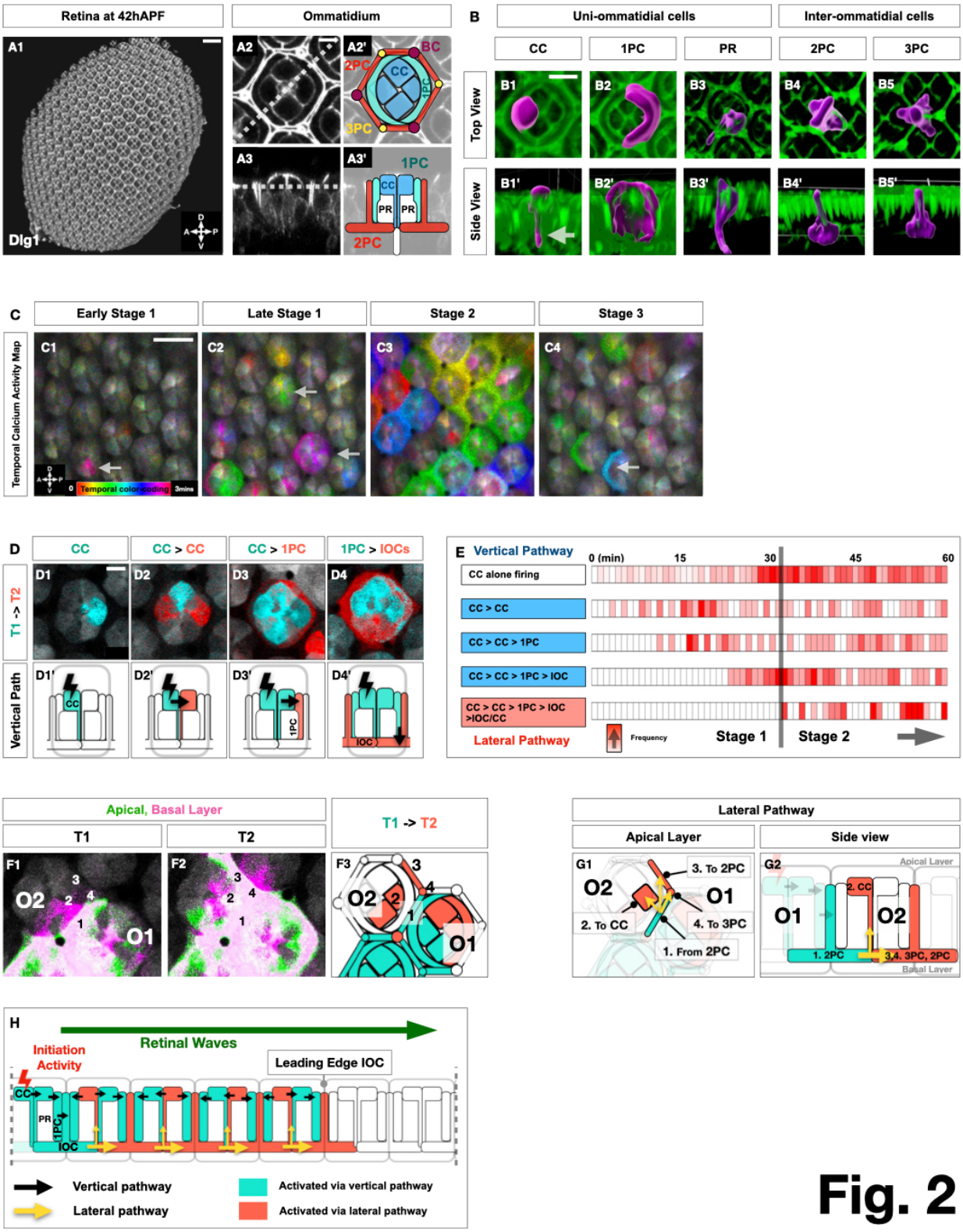
Retina at 42hAPF
Ommatidium
A1
Dlg1
A2
A2'
BC
2PC
CC
1PC
3PC
A3
A3'
1PC
CC
PR
PR
2PC
B
Uni-ommatidial cells
Inter-ommatidial cells
CC
1PC
PR
2PC
3PC
Top View
Side View
B1
B2
B3
B4
B5
B1'
B2'
B3'
B4'
B5'
C
Early Stage 1
Late Stage 1
Stage 2
Stage 3
Temporal Calcium Activity Map
C1
C2
C3
C4
Temporal color-coding
3mins
D
CC
CC > CC
CC > 1PC
1PC > IOCs
T1 -> T2
Vertical Path
D1
D2
D3
D4
D1'
D2'
D3'
D4'
CC
1PC
IOC
E
Vertical Pathway
0 (min)
15
30
45
60
CC alone firing
CC > CC
CC > CC > 1PC
CC > CC > 1PC > IOC
CC > CC > 1PC > IOC >IOC/CC
Lateral Pathway
Frequency
Stage 1
Stage 2
Apical, Basal Layer
T1
T2
T1 -> T2
F1
F2
F3
O2
O1
Lateral Pathway
Apical Layer
Side view
G1
G2
3. To 2PC
2. To CC
4. To 3PC
1. From 2PC
2. CC
1. 2PC
3,4. 3PC, 2PC
Apical Layer
Basal Layer
H
Retinal Waves
Initiation Activity
Leading Edge IOC
CC
PR
1PC
IOC
Vertical pathway
Lateral pathway
Activated via vertical pathway
Activated via lateral pathway

Fig. 2

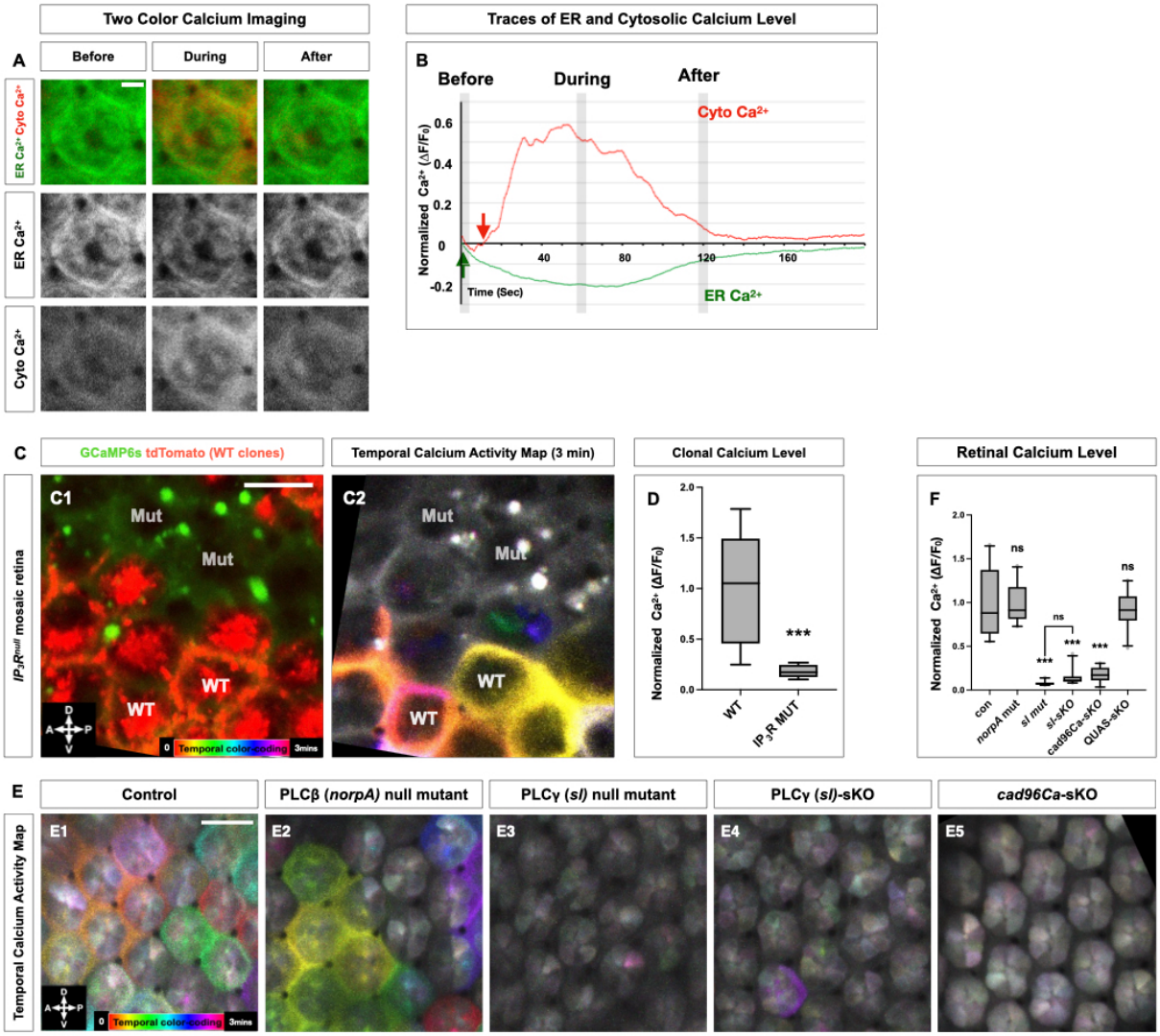
Two Color Calcium Imaging
A
Before
During
After
ER Ca2+ Cyto Ca2+
ER Ca2+
Cyto Ca2+
Traces of ER and Cytosolic Calcium Level
B
Before
During
After
Cyto Ca2+
ER Ca2+
Normalized Ca2+ (ΔF/F0)
Time (Sec)
C
GCaMP6s tdTomato (WT clones)
Temporal Calcium Activity Map (3 min)
Clonal Calcium Level
Retinal Calcium Level
IP3Rnull mosaic retina
C1
C2
Mut
WT
Temporal color-coding
3mins
D
WT
IP3R MUT
F
con
norpA mut
sl mut
sl-sKO
cad96Ca-sKO
QUAS-sKO
ns
E
Control
PLCβ (norpA) null mutant
PLCγ (sl) null mutant
PLCγ (sl)-sKO
cad96Ca-sKO
Temporal Calcium Activity Map
E1
E2
E3
E4
E5

Fig. 3

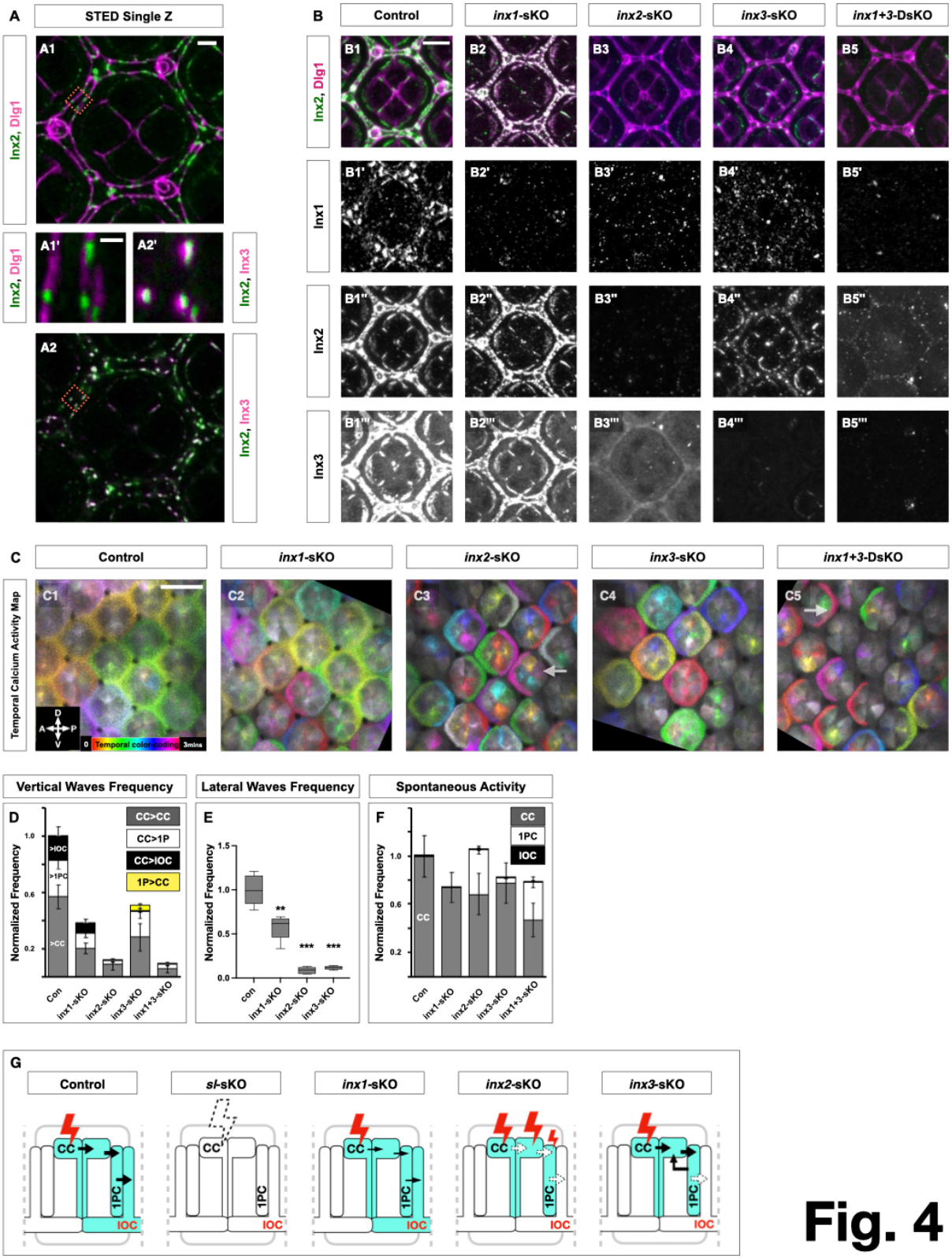
A
STED Single Z
Inx2, Dlg1
A1
A1'
A2'
Inx2, Inx3
A2
B
Control
inx1-sKO
inx2-sKO
inx3-sKO
inx1+3-DsKO
Inx1
Inx2
Inx3
C
Temporal Calcium Activity Map
C1
C2
C3
C4
C5
Temporal color coding
3mins
Vertical Waves Frequency
Lateral Waves Frequency
Spontaneous Activity
D
E
F
Normalized Frequency
CC>CC
CC>1P
CC>IOC
1P>CC
CC
1PC
IOC
Con
inx1-sKO
inx2-sKO
inx3-sKO
inx1+3-sKO
G
Control
sl-sKO
inx1-sKO
inx2-sKO
inx3-sKO
CC
1PC
IOC

Fig. 4

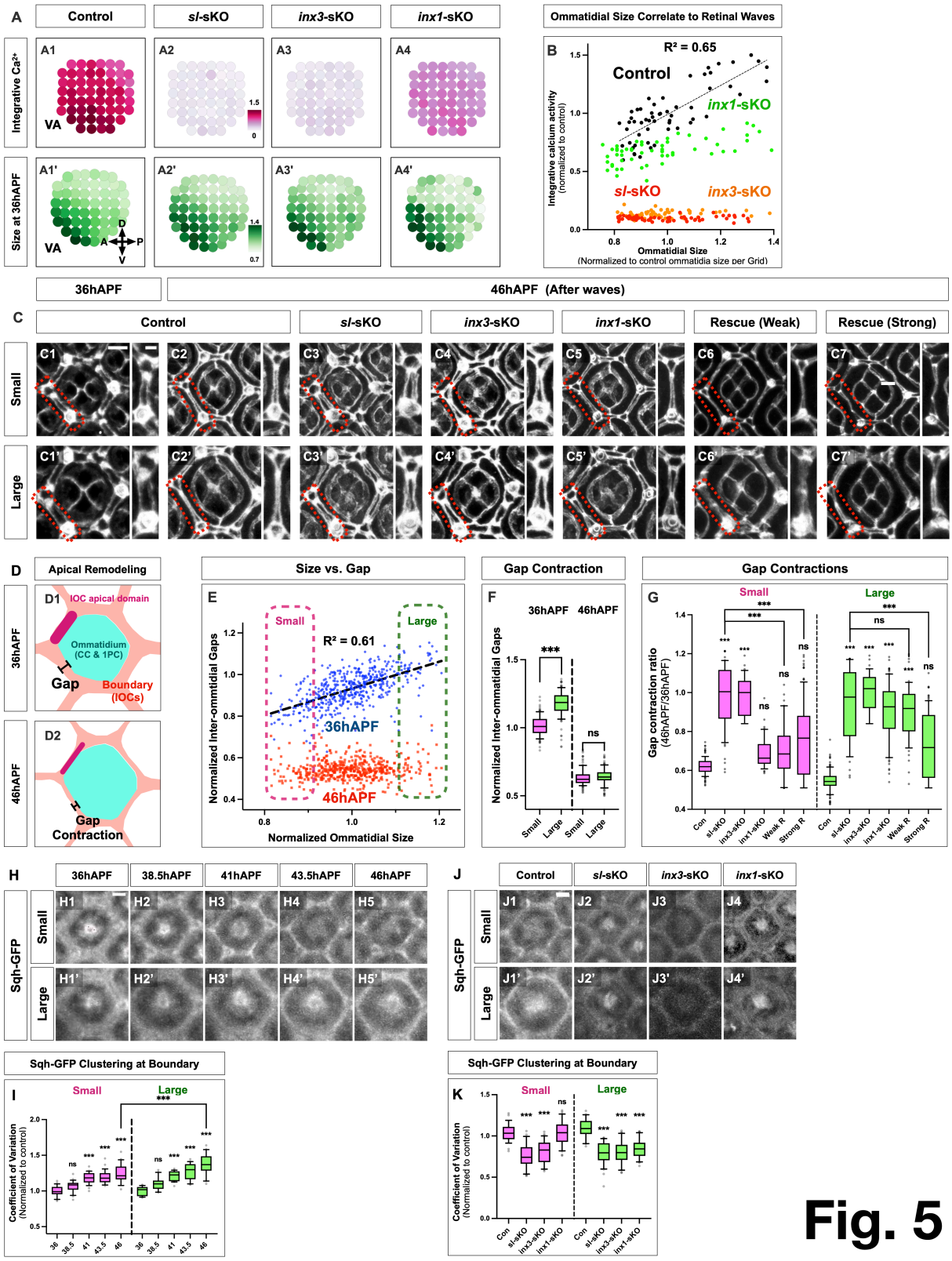
A
Control
sl-sKO
inx3-sKO
inx1-sKO
Integrative Ca2+
Size at 36hAPF
A1
A2
A3
A4
A1'
A2'
A3'
A4'
VA
D
A
P
V
Ommatidial Size Correlate to Retinal Waves
B
R² = 0.65
Control
inx1-sKO
sl-sKO
inx3-sKO
Integrative calcium activity (normalized to control)
Ommatidial Size
(Normalized to control ommatidia size per Grid)
36hAPF
46hAPF (After waves)
C
Control
sl-sKO
inx3-sKO
inx1-sKO
Rescue (Weak)
Rescue (Strong)
Small
Large
C1
C2
C3
C4
C5
C6
C7
C1'
C2'
C3'
C4'
C5'
C6'
C7'
D
Apical Remodeling
36hAPF
46hAPF
D1
IOC apical domain
Ommatidium (CC & 1PC)
Gap
Boundary (IOCs)
D2
Gap Contraction
Size vs. Gap
E
Small
Large
R² = 0.61
36hAPF
46hAPF
Normalized Inter-ommtidial Gaps
Normalized Ommatidial Size
Gap Contraction
F
36hAPF 46hAPF
Normalized Inter-ommatidial Gaps
Small
Large
Gap Contractions
G
Small
Large
Gap contraction ratio (46hAPF/36hAPF)
Con
sl-sKO
inx3-sKO
inx1-sKO
Weak R
Strong R
H
36hAPF
38.5hAPF
41hAPF
43.5hAPF
46hAPF
Sqh-GFP
H1
H2
H3
H4
H5
H1'
H2'
H3'
H4'
H5'
J
J1
J2
J3
J4
J1'
J2'
J3'
J4'
Sqh-GFP Clustering at Boundary
I
Coefficient of Variation (Normalized to control)
K

Fig. 5

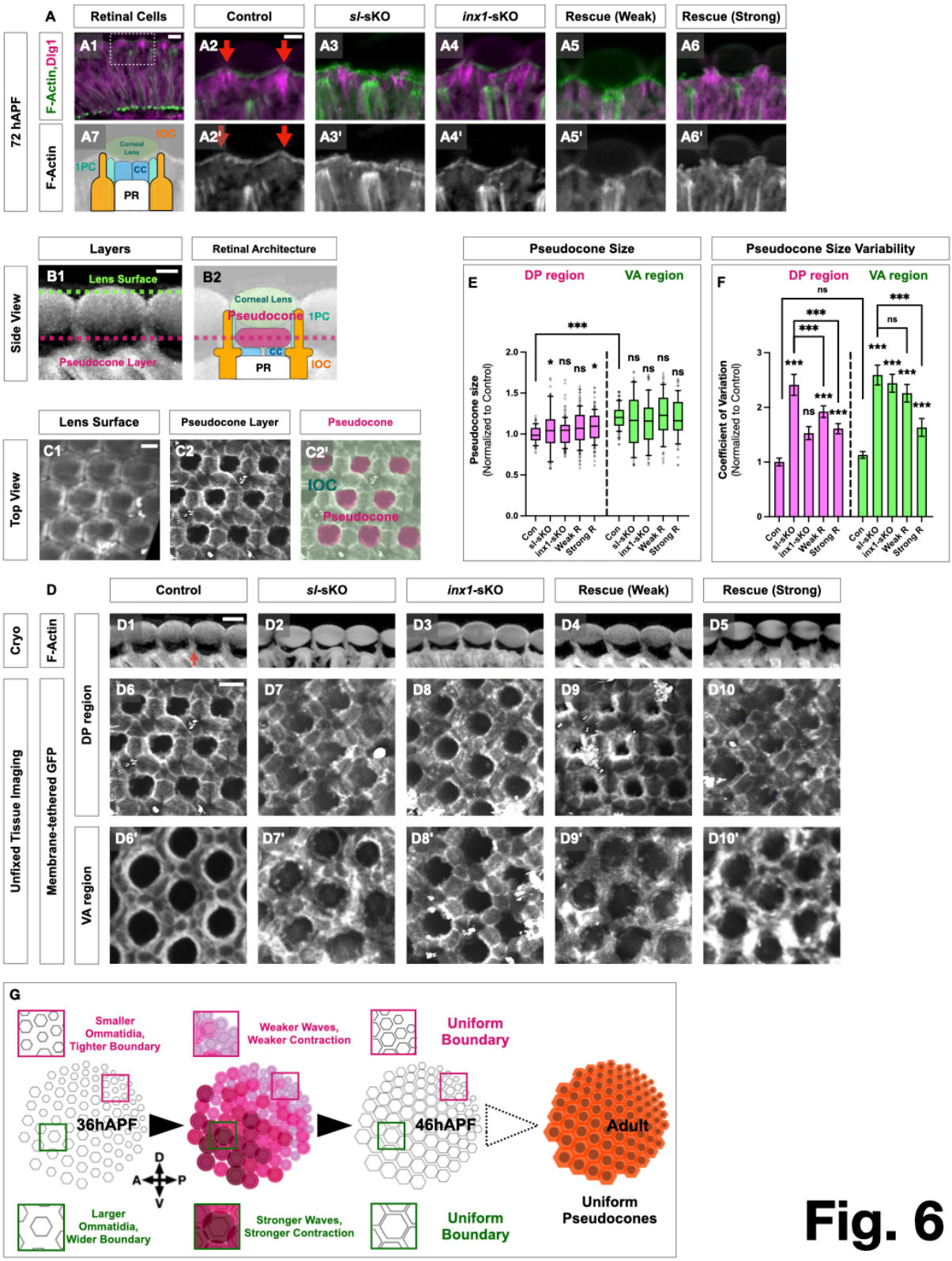
A
Retinal Cells
Control
sl-sKO
inx1-sKO
Rescue (Weak)
Rescue (Strong)
72 hAPF
F-Actin,Dlg1
F-Actin
Corneal Lens
IOC
1PC
CC
PR
Layers
Retinal Architecture
Side View
Lens Surface
Pseudocone Layer
Pseudocone
Top View
Pseudocone Size
Pseudocone Size Variability
DP region
VA region
Pseudocone size (Normalized to Control)
Coefficient of Variation (Normalized to Control)
Con
sl-sKO
inx1-sKO
Weak R
Strong R
D
Cryo
Unfixed Tissue Imaging
Membrane-tethered GFP
G
Smaller Ommatidia, Tighter Boundary
Weaker Waves, Weaker Contraction
Uniform Boundary
36hAPF
46hAPF
Adult
Larger Ommatidia, Wider Boundary
Stronger Waves, Stronger Contraction
Uniform Pseudocones

Fig. 6

FIGURE TITLES AND LEGENDS

Fig. 1. Early retinal calcium waves in the developing retina (A–I).

1A. Imaging platform of intact pupa with dry lens setup **(A1)**, sample preparation **(A2)**, and representative retinal calcium imaging **(A2')**. Red box indicates imaging area for **(C)**. Scale bar: 500 µm (**A2, A2'**).

1B. Trace of average retinal calcium dynamics throughout pupal retinal development. Calcium imaging was performed at 2-minute intervals and n≧5 retinas were analyzed for each time window. Detailed shown in **Fig. S1A**, **Video S1**.

1C. Representative images of retinal calcium wave activity, displayed as color-coded 5-minute temporal activity maps (T-stack) for the pre-wave phase **(C1),** stage 1 **(C2),** stage 2 **(C3)**, and stage 3 **(C4)** of *longGMR-GAL4>UAS-GCaMP6s* retina. Arrow in **(C1)** indicates single cone cell firing and arrowhead in **(C2)** indicates full firing of ommatidium. All images came from the same retina and calcium imaging was performed at 3-second intervals. A = anterior, P = posterior, D = dorsal, V = ventral. Scale bar: 20 µm (**C1–C4**).

1D. Individual traces of retinal calcium activity as in **(1C)**. 5 individual retina is labeled with different color and the black trace represents average retinal calcium levels.

1E. Quantification of the timing of the onset of retinal waves. n = 19. Error bars represent SD.

1F. Quantification of the duration of retinal waves. n = 19. Error bar indicates SD.

1G. Ommatidial-level retinal wave-induced integrative calcium activity between 37hAPF and 41hAPF. Each bin represents a 30-minute time period, and each hexagon represents a single ommatidium. The level of integrative calcium signal for individual ommatidium during each 30-minute time window is color-coded. All images came from the same retina as in Fig. 1C.

1H. Population data using an ommatidial configuration grid of ommatidial-level wave activity. Each circle represents a group of ommatidia activity located within an 8x8 grid along the DorsoVentral (DV) and anterio-posterior (AP) axes. The average level of integrative calcium activity during the entire wave period is color-coded. Data combined from 6 control retinas.

1I. Quantification of ommatidial-level integrative calcium activity between different retinal quadrants shown in **Fig. 1H**. n ≧ 432 ommatidia from 6 retinas, ns: $p \geq 0.05$, * : $p < 0.05$, *** : $p < 0.001$. Error bars represent SD.

Fig. 2: Single cell resolution of retinal waves reveals stereotyped patterns of initiation and propagation (A-H).

2A. Representative images of an entire retina (**A1**) and single ommatidium (**A2, A3**) immunostained with the junctional marker Dlg1. **A2:** apical side; **A3:** Cross-section where the dotted line in **A2** indicates the cutting plane for **A3**, and the dotted line in **A3** indicates the cutting plane for **A2**. **A2', A3':** Representations of the retinal cell types: cone cell (**CC**), primary pigment cell (**1PC**), secondary pigment cell (**2PC**), tertiary pigment cell (**3PC**), bristle cell (**BC**), and photoreceptor (**PR**). Scale bar: 20 µm (**A1**), 5 µm (**A2, A3**).

2B. Three-dimensional reconstructions of individual retinal cell morphology of *longGMR-GAL4>UAS-MCFO* retina at 40 hAPF. Top views (**B1–5**) and side views (**B1'–5'**) reveal cellular architecture. Magenta marks single-cell labeling with a membrane-tethered ectopic tag, while green marks the junctional marker Dlg1. The arrow in **B1'** highlights the leg-like structure of the CC contacting IOCs. Scale bar: 10 µm (**B1–5**).

2C. Representative images of retinal calcium wave activity at single-cell resolution, displayed as color-coded 3-minute temporal activity maps across different developmental stages: early stage 1 (**C1**), late stage 1 (**C2**), stage 2 (**C3**), and stage 3 (**C4**) of *longGMR-GAL4>UAS-GCaMP6s*

retina. The arrow in **C1** indicates single cone cell firing. Arrows in **C2** indicate vertical waves. Arrow in **C4** indicates single primary pigment cell firing. All images come from the same retina. Scale bar: 10 μm (**C1–C4**).

2D. Wave patterns of the vertical pathway, including single CC firing (**D1**), CC to CC propagation (**D2**), CC to 1PC propagation (**D3**), and CC to IOC propagation (**D4**). The first time (**T1**, cyan) and 4-seconds later (**T2**, red). **D1'–4'** are schematic representations. Scale bar: 5 μm (**D1–4**).

2E. Event log of retinal waves during stage 1 and the initial part of stage 2, with each bin representing a one-minute interval and event frequency highlighted in red-color coding. Blue box: vertical propagation pathway; red box: lateral propagation pathway.

2F. Wave patterns in the lateral pathway. **F1, F2:** T-series images with apical (green) and basal (magenta) layers. The time interval between **T1** and **T2** is 4 seconds. **1–4** indicate the following retinal cells: initial 2PC (**1**), propagated CC (**2**), 3PC (**4**), and 2PC (**3**). **F3:** Schematic representations of calcium signaling at two time points, **T1** (cyan) and **T2** (red). Scale bar: 5 μm (**F1, F2**).

2G. Diagram of wave patterns in the lateral pathway as in **2F**.

2H. Diagram of retinal waves propagation along the two pathways across multiple ommatidia.

Fig. 3: Cad96Ca-PLCγ-IP$_3$R signaling triggers calcium release from the ER, inducing retinal wave initiation (A-F).

3A. Time-lapse images of dual-color calcium imaging captured before, during the peak, and after retinal waves. Each image is selected at 60-second intervals to represent calcium dynamics. Calcium imaging was performed at a one-second interval at the center of the retina during wave stage 2. Scale bar: 5 μm.

3B. Traces of calcium activity during retinal waves. The shaded regions correspond to the timings of the snapshots shown in **3A**. Red trace: cytosolic jRgeco1a; green: ER-located GCaMP6. Arrows indicate when calcium waves start in each channel.

3C. Retinal waves in *IP$_3$R* mutant mosaic retinas. **C1:** RFP cells are wild-type (**WT**) while non-labelled cells are mutant for *IP$_3$R* (**Mut**). **C2:** 3-minute T-stacks of temporal color-coded calcium imaging using *longGMRG4>UAS-GCaMP8s* with mutant mosaic retina. Scale bar: 10 μm (**C1, C2**).

3D. Quantitative calcium activity of individual ommatidia made by WT or Mut clones from *IP$_3$R* mosaic retinas. n ≧ 15 ommatidia from 5 retinas, ***: $p < 0.001$. Error bars represent SD.

3E. Representative images of retinal calcium wave activity, displayed as color-coded 3-minute temporal activity maps in control (**E1**), *norpA* mutants (**E2**), *sl* mutants (**E3**), *sl*-sKO (**E4**), and *cad96Ca*-sKO (**E5**). **sKO = somatic CRISPR knockout.** Scale bar: 10 μm (**E1–5**).

3F. Quantification of retinal wave calcium activity from **3E**. n ≧ 7 retinas, ns: $p \geq 0.5$, $p < 0.001$. Error bars represent SD.

Fig. 4: Retinal waves propagate through gap-junctions using cell-type specific combinations of Innexins (A-G).

4A. Stimulated Emission Depletion (STED) imaging of the same single ommatidium at 40hAPF immunostained for Dlg1 and Inx2 (**A1, A1'**) or Inx2 and Inx3 (**A2, A2'**). Insets from **A1** and **A2** (see red box). Scale bar: 2 μm (**A1, A2**), 0.5 μm (**A1', A2'**).

4B. Immunostaining for Inx1, Inx2, and Inx3 at 40hAPF from control (**B1, B1', B1'', B1'''**), *inx1*-sKO (**B2, B2', B2'', B2'''**), *inx2*-sKO (**B3, B3', B3'', B3'''**), *inx3*-sKO (**B4, B4', B4'', B4'''**), and *inx1+3*-double sKO (**B5, B5', B5'', B5'''**) retinas. Corresponding Innexins labeled

as green and apical cell junction Dlg1 as magenta. The images are Z-stacks of the retinal apical layer. Scale bar: 5 μm (**B1–5**).
4C. Representative images of retinal calcium wave activity, displayed as color-coded 3-minute temporal activity maps from control (**C1**), *inx1*-sKO (**C2**), *inx2*-sKO (**C3**), *inx3*-sKO (**C4**), and *inx1+3*-DsKO (**C5**) retinas during stage 2. Arrows in **C3, C5** indicate unsynchronized firing of adjacent cone cells and primary pigment cells. Scale bar: 10 μm (**C1–5**).
4D. Quantification of the frequency of vertical pathway in *inx* mutant retinas during stage 2. n ≥ 5 retinas, error bars represent SD, and detailed statistics results are available in **Fig. S4J**.
4E. Quantification of the frequency of lateral pathway in *inx* mutant retinas during stage 2. n ≥ 5 retinas, ns: $p \geq 0.5$, **: $p < 0.01$, ***: $p < 0.001$. Error bars represent SD.
4F. Quantification of the frequency of spontaneously emerging cell-autonomous activity from each cell type in *inx* mutant retinas during stage 1. n ≥ 5 retinas, error bars represent SD, and detailed statistics results are available in **Fig. S4J**.
4G. Diagram illustrating the vertical propagation pathway of *inx* mutant retinas.

Fig. 5. Retinal waves instruct uniform ommatidial packing via Myosin II-driven apical remodeling by scaling with ommatidial size (A-K).
5A. Population data using an 8×8 grid to display integrated calcium signals from retinal waves (**A1–A4**) and ommatidial size distribution (**A1'–A4'**) for corresponding control and mutant retinas. The average level of integrative calcium signal and ommatidial size per grid points are color-coded in magenta and green, respectively. n ≥ 11 retinas.
5B. Scatter plot of normalized ommatidial size (X-axis) versus integrated calcium signals (Y-axis). Each dot represents an individual grid point from the 8×8 grid in **5A**, with genotype color-coded as shown in the inset. The black line represents linear regression for the control retina.
5C. Representative Dlg1 immunostaining of single ommatidium at 36hAPF and 46hAPF, marking apical junctions. **C1–7** show small ommatidia (0–20%) from dorsal-posterior region, and **C1'–7'** show large ommatidia (80–100%) from ventral-anterior region for indicated genotypes. Red insets highlight individual inter-ommatidial boundary gap, enlarged in the side insets. Scale bar: 5 μm (**C1–7, C1'–7'**), 2 μm (Side insets).
5D. Diagram illustrating ommatidial apical remodeling during retinal waves, depicting ommatidium at 36hAPF (**D1**) and 46hAPF (**D2**). Black distance lines in the inter-ommatidial boundary indicate apical gaps measured for quantification.
5E. Scatter plot of ommatidial size (X-axis) versus inter-ommatidial gap (Y-axis) at 36hAPF (blue) and 46hAPF (red) from immunostained images using Dlg1 (**5C**). Each dot represents an individual ommatidium, where the Y value corresponds to the average inter-ommatidial gaps surrounding that ommatidium. All values are normalized to the average value of ommatidia at 36hAPF. The black line shows the regression for 36hAPF ommatidia. n ≥ 497 ommatidia from n ≥ 16 retinas per stage. Dashed boxes indicate size groups for **Fig. 5F**.
5F. Quantification of inter-ommatidial gaps in different size groups at 36hAPF and 46hAPF (**5E**) from Dlg1 immunostaining (**5C**). n ≥ 105 ommatidia from n ≥ 16 retinas per stage, ns: $p \geq 0.05$, ***: $p < 0.001$. Error bars represent SD.
5G. Quantification of the gap contraction ratio between 36hAPF and 46hAPF for small (magenta) and large (green) size groups of ommatidia using Dlg1 immunostaining (**5C**). The Y-axis shows the gap contraction ratio, calculated as the ratio of inter-ommatidial gap size at 46hAPF to the gap size at 36hAPF for each group. n ≥ 105 ommatidia from n ≥ 16 retinas per size group, ns: $p \geq 0.05$, ***: $p < 0.001$. Error bars represent SD.

5H. Representative time-lapse images of a single ommatidium from 36hAPF to 46hAPF, taken at 2.5-hour intervals, showing Sqh-GFP puncta. **H1–5** show small ommatidia, and **H1'–5'** show large ommatidia at different time points. Scale bar: 5 μm (**H1–5, H1'–5'**).
5I. Quantification of the coefficient of variation of Sqh-GFP within inter-ommatidial boundary between 36hAPF and 46hAPF from time-lapse imaging (**5H**). n ≥ 25 ommatidia from n ≥ 5 retinas per genotype, ns: p ≥ 0.05, **: p < 0.01, ***: p < 0.001. Error bars represent SD.
5J. Representative images of a single ommatidium with Sqh-GFP puncta from retina at 46hAPF. **J1–4** show small ommatidia, and **J1'–4'** show large ommatidia for the indicated genotype. Scale bar: 5 μm (**J1–4, J1'–4'**).
5K. Quantification of the coefficient of variation of Sqh-GFP within inter-ommatidial boundary at 46hAPF from **5J**. n ≥ 22 ommatidia from n ≥ 4 retinas per genotype, ns: p ≥ 0.05, ***: p < 0.001. Error bars represent SD.

Fig. 6. Retinal wave activity ensures eye uniformity in adults (A-G).
6A. Representative images of 72hAPF retinal surfaces obtained via confocal imaging of cryosections from a side view labeled with phalloidin (green for **A2–6**, grey for **A2'–6'**) and Dlg1 (magenta) to mark actin filaments and cell junctions, respectively. Red arrows in A2 indicate primitive lens footings formed by IOC tips. **A1** shows the whole retina section, with an inset of the apical surface in **A2**. **A7** represents a diagram of the retinal cellular configuration, with cell types labeled and color-coded consistently with **6B2**. For cryosection, we focused on the dorsal-posterior region for optimal sectioning. Z-stack thickness: 5 μm. Scale bar: 10 μm **(A1),** 5 μm **(A2–7, A2'–7').**
6B. Diagram illustrating the cellular architecture of the adult eye's retinal surface from a side view showing the optical layer corresponding to **6D1–5**. Scale bar: 5 μm **(B1, B2).**
6C. Representative images (**C1, C2**) and diagram (**C2'**) illustrating the cellular architecture of the adult eye's retinal surface from a top view showing optical layers corresponding to **6D6–10**. **C2':** Diagram illustrating the shape and size of pseudocones (magenta), with IOCs labeled in green. Scale bar: 10 μm **(C1, C2).**
6D. Representative images of adult retinal surfaces from a side view (**D1–5**) and a top view (**D6–10**). **D1–5:** Confocal images of cryosections labeled with phalloidin to mark actin filaments. Red arrows indicate lens footings in D1. Z-stack thickness: 5 μm. For cryosection, we focused on the dorsal-posterior region for optimal sectioning. **D6–10** (Dorsal-posterior or DP region)**, D6'–10'** (Ventral-anterior or VA region)**:** Two-photon images of unfixed adult retinas labeled with membrane-tethered GFP, focusing on the pseudocone layer (shown in **6C2**). Optical Z-stack thickness: 10 μm. Scale bar: 10 μm **(D1–10, D7'–10').**
6E. Quantification of pseudocone size from **6D** normalized to control. n ≥ 104 pseudocones from ≥ 15 retinas per genotype. ns: p ≥ 0.05, *: p < 0.05. Error bars represent SD.
6F. Quantification of pseudocone size variability from **6D**, measured using the coefficient of variation. n ≥ 104 pseudocones from ≥ 15 retinas per genotype. Statistical significance was tested using a bootstrap t-test. Error bars represent standard error calculated from bootstrap resampling. ns: p ≥ 0.5, ***:p < 0.001.
6G. Summary diagram illustrating how retinal waves coordinate uniform pseudocone formation in the adult eye through apical remodeling scaled by ommatidial size. At 36hAPF, the retina exhibits regional ommatidial size variation, accompanied by inter-ommatidial gap differences. Retinal waves promote regional calcium signaling proportionate to ommatidial size, which induces dose-dependent inter-ommatidial gap contraction. This compensating process ensures the formation of uniform ommatidial boundaries by 46hAPF, which are essential for uniform pseudocone development in the adult retina.

Materials and Methods

Materials

REAGENT OR RESOURCE	SOURCE	IDENTIFIER
Antibodies		
Chicken Anti-GFP	Millipore Sigma	Catalog #06-896; RRID: AB_310288
Rabbit Anti-HA	Cell Signaling Technologies	Catalog #C29F4; RRID: AB_10693385
Rat Anti-Flag	Novus Biologicals	Catalog #NBP1-06712; RRID: AB_1625981
Mouse Anti-V5-tag:DyLight550	Bio-Rad	Catalog #MCA1360D550GA; RRID: AB_2687576
Mouse Anti-Dlg1	DSHB	4F3; RRID: AB_528203
Mouse Anti-Ecad	DSHB	DCAD2: RRID: AB_528120
Mouse Anti-Coracel	DSHB	C566.9: RRID: AB_1161642
Rabbit Anti-Inx1	M. Hoch	Richard et al., 2017
Rabbit Anti-Inx2	M. Hoch	Richard et al., 2017
Rabbit Anti-Inx1	A. Borst	Ammer et al., 2022
Rabbit Anti-Inx2	A. Borst	Ammer et al., 2022
Rabbit Anti-Inx4	A. Borst	Ammer et al., 2022
Rabbit Anti-Inx5	A. Borst	Ammer et al., 2022
Rabbit Anti-Inx6	A. Borst	Ammer et al., 2022
Rabbit Anti-Inx7	A. Borst	Ammer et al., 2022
Rabbit Anti-Inx8	A. Borst	Ammer et al., 2022
Guinea Pig Anti-Inx1	This study	N/A
Guinea Pig Anti-Inx3	This study	N/A
AlexaFluor647 conjugated Goat Anti-HRP	Jackson ImmunoResearch	Code #123-605-021; RRID: AB_2338967
Donkey Anti Rat 405	Jackson ImmunoResearch	Code # 712-475-150; RRID: AB_2340680
Donkey Anti Chicken A488	Jackson ImmunoResearch	Code #703-545-155; RRID: AB_2340375
Donkey Anti Mouse A488	Jackson ImmunoResearch	Code #715-545-151; RRID: AB_2341099
Donkey Anti Rabbit A488	Jackson ImmunoResearch	Code #711-545-152; RRID: AB_2313584
Donkey Anti Mouse A555	Thermo Scientific	Catalog #A-31570; RRID: AB_2536180
Donkey Anti Rabbit A555	Thermo Scientific	Catalog #A-31572; RRID: AB_162543
Donkey Anti Guinea pig A647	Jackson ImmunoResearch	Code #706-605-148; RRID: AB_2340476
Donkey Anti Mouse A647	Jackson ImmunoResearch	Code #715-605-151; RRID: AB_2340863
Chemicals, peptides, and recombinant proteins		
SlowFade Gold	Thermo Scientific	Catalog #S36936
Experimental models: Organisms/strains : Fly: ***D. melanogaster***		
y[1] w[*]; wg[Sp-1]/CyO; P{w[+mC]=longGMR-GAL4}3 (or **longGMR-GAL4)**	Bloomington	Stock # 8121
w[*]; P{w[+mC]=GAL4-ninaE.GMR}12 (or **GMR-GAL4**)	Bloomington	Stock # 1104
w[1118]; P{y[+t7.7] w[+mC]=20XUAS-IVS-GCaMP6s}attP40 (or **UAS-GCaMP6s)**	Bloomington	Stock # 42746

w[*]; PBac{y[+mDint2] w[+mC]=20XUAS-IVS-NES-jRGECO1a-p10}VK00005/TM6B, Tb[1] (or **UAS-jRgeco1a**)	Bloomington	Stock # 63794
w[*]; P{y[+t7.7] w[+mC]=UAS-ER.GCaMP6-210}su(Hw)attP5; TM2/TM6B, Tb[1] (or **UAS-ER-GCaMP6**)	Bloomington	Stock # 83294
w[1118] P{y[+t7.7] w[+mC]=hs-FLPG5.PEST}attP3; PBac{y[+mDint2] w[+mC]=10xUAS(FRT.stop)myr::smGdP-HA}VK00005 P{y[+t7.7] w[+mC]=10xUAS(FRT.stop)myr::smGdP-V5-THS-10xUAS(FRT.stop)myr::smGdP-FLAG}su(Hw)attP1 (or **MCFO**)	Bloomington	Stock # 64085
P{ey-FLP.N}5	Bloomington	Stock # 5576
w[1118]; P{y[+t7.7] w[+mC]=20XUAS-IVS-jGCaMP8s}su(Hw)attP5 (or **UAS-GCaMP8s**)	Bloomington	Stock # 92594
w[1118]; P{ry[+t7.2]=neoFRT}82B P{w[+mC]=GMR-myr-mRFP}3R/TM6B, Tb[1]	Bloomington	Stock # 7124
Itpr[90B.0]/TM6B, Tb[1] (or ***IP_3R^{mut}***)	Bloomington	Stock # 30737
w[*] norpA[P24] (or ***$norpA^{mut}$***)	Bloomington	Stock # 9048
y[1] v[1] sl[KO]/FM7c (or ***sl^{mut}***)	Bloomington	Stock # 93748
w[*]; P{y[+t7.7] w[+mC]=10XUAS-IVS-myr::GFP}attP40 (or **UAS-myrGFP**)	Bloomington	Stock # 32198
w[*]; P{y[+t7.7] w[+mC]=UAS-TrpA1(B).K}attP16 (or **UAS-TrpA**)	Bloomington	Stock # 26263
w[1118]; P{w[+mC]=sqh-GFP.RLC}3 (or **Sqh-GFP**)	Bloomington	Stock # 57145
w[1118]; P{y[+t7.7] w[+mC]=10XUAS-IVS-myr::GFP}su(Hw)attP1/TM3, Sb[1]	Bloomington	Stock # 32200
y[1] w[*]; Mi{Trojan-GAL4.1}Cad96Ca[MI05299-TG4.1p] CG13654[MI05299-TG4.1p-X]/TM3, Sb[1] Ser[1] (or **cad96Ca-GAL4**)	Bloomington	Stock # 76669
y[1] sc[*] v[1] sev[21]; P{y[+t7.7] v[+t1.8]=TRiP.HMS02764}attP2	Bloomington	Stock # 44048
y[1] sc[*] v[1] sev[21]; P{y[+t7.7] v[+t1.8]=TKO.GS01151}attP40	Bloomington	Stock # 78592
w[1118]; P{y[+t7.7] w[+mC]=UAS-Cas9.C}attP2	Bloomington	Stock # 54595
y[1] w[*]; P{w[+m*]=GAL4}54C	Bloomington	Stock # 27328
Canton-S	Desplan Lab/ originally from M. Heisenberg	N/A
w;;Chaoptin-GAL4	Desplan Lab/ originally from S. Sprecher	https://flybase.org/reports/FBal0303652
w[1118]; P{w[+mC]=GMR-GCaMP6s}attP40	This study	N/A
w[1118], P{w[+mC]=longGMR-Cas9}attP4 (or **longGMR-Cas9**)	This study	N/A
w[1118]; P{w[+mC]=pCFD5w-6xgRNA-inx1}attP40 (or **gRNA-inx1[6x]**)	This study	N/A
w[1118]; P{w[+mC]=pCFD5w-6xgRNA-inx2}attP40 (or **gRNA-inx2[6x]**)	This study	N/A
w[1118]; P{w[+mC]=pCFD5w-6xgRNA-inx3}attP40 (or **gRNA-inx3[6x]**)	This study	N/A
w[1118]; P{w[+mC]=pCFD5w-6xgRNA-sl}attP40 (or **gRNA-sl[6x]**)	This study	N/A
w[1118]; P{w[+mC]=pCFD5w-6xgRNA-Cad96Ca}attP40 (or **gRNA-cad96Ca[6x]**)	This study	N/A
w[1118]; P{w[+mC]=pCFD5w-6xgRNA-dnt}attP40	This study	N/A
w[1118]; P{w[+mC]=pCFD5w-6xgRNA-drl}attP40	This study	N/A
w[1118]; P{w[+mC]=pCFD5w-6xgRNA-eph}attP40	This study	N/A
w[1118]; P{w[+mC]=pCFD5w-6xgRNA-otk}attP40	This study	N/A
w[1118]; P{w[+mC]=pCFD5w-6xgRNA-pvr}attP40	This study	N/A
w[1118]; P{w[+mC]=pCFD5w-6xgRNA-tie}attP40	This study	N/A
w[1118]; P{w[+mC]=pCFD5w-6xgRNA-tor}attP40	This study	N/A
w[1118]; P{w[+mC]=pCFD5w-6xgRNA-QUAS}attP40	This study	N/A

w[1118];; P{w[+mC]=pCFD5w-6xgRNA-inx1}attP5	This study	N/A
Software and algorithms		
Fiji	RRID: SCR_002285	https://fiji.sc
Imaris	RRID:SCR_007370	http://www.bitplane.com/imaris/imaris
Microsoft Excel	RRID: SCR_016137	https://www.microsoft.com/en-us/microsoft-365/excel
R (v4.2.0)	RRID: SCR_001905	https://cran.r-project.org/
GraphPad Prism	RRID: SCR_002798	https://www.graphpad.com/

Methods

***Drosophila* melanogaster Strains and Husbandry:** All *Drosophila melanogaster* stocks used are listed in the Key Resources Table. Flies were reared on standard cornmeal medium under 12-hour light/dark cycles at 25°C, unless specified otherwise. Only male flies were analyzed to take advantage of enhanced efficacy of somatic knock-out of major target genes (*sl*, *inx1*, *inx2*) located on the X chromosome. Pupal staging was performed by marking white pupae adhered to the dry wall of the vial, defined as 0hAPF (hours after puparium formation). Pupae exhibiting significantly smaller body size were excluded from all experiments. Detailed genotypes corresponding to each figure are provided in Table S2.

Generation of Transgenic Animals: Transgenic constructs including longGMR-Cas9, customized guide RNAs, and GMR-GCaMP6s were generated by GenScript (Piscataway, NJ, USA). Insertions were synthesized into appropriate plasmid backbones (**see Table S3** for plasmid details). All transgenes were injected into corresponding attP sites by TheBestGene (Chino Hills, CA, USA) (**see Materials** for transgene information). For guide RNAs, we used the pCFD5_w vector (*56*) with the U6:3 promoter to ubiquitously express six tandem guide RNAs, consisting of two duplicated sets targeting three selected sites within the first and second common exons (see **Table S3** for guide RNA details). This configuration produced a strong somatic knock-out effect across all tested targets, as shown in Figure S5F.

Live Imaging of Intact Pupal Retina: Pupae within the selected developmental window were gently attached to double-sided tape (Scotch) on a slide in the desired position. The pupal case surrounding the head was minimally removed using fine-tip forceps without touching or pulling the pupal body. Samples were imaged using dry-objective lenses with a semi-open chamber surrounded by wet Kimwipes, utilizing either a Leica SP8 confocal microscope or an Olympus FV1000MPE2 two-photon microscope. Imaging was performed using 488 nm (confocal, Leica SP8) or 920 nm (two-photon, Olympus FV1000MPE2; Mai Tai Ti:Sapphire Lasers) excitation lasers.
All images were acquired with a 10x Leica dry objective (confocal) or a 20x Olympus dry objective (two-photon)**.** For confocal imaging, the entire retina was scanned using a 10x objective with 3x zoom**.** For two-photon imaging, the flattest local area of each mounted retina, between the central and dorsal retinal regions, was scanned using a 20x objective with 8x zoom**.** Images were collected using LAS-X (Leica) at 1024 × 800 pixel resolution or Fluoview (Olympus) at 512 × 512 pixel resolution. Laser power was adjusted to the minimum necessary to avoid potential phototoxicity and photobleaching.

Images displaying ectopic local or global increases in basal calcium levels during scanning (indicating potential phototoxicity) or significant reductions in basal calcium levels (indicating abnormal photobleaching) were excluded from further analysis.
Each scanning session lasted up to 12 hours for any analysis to avoid potential phototoxicity. After successful imaging, animals were returned to standard fly food with wet Kimwipes. Successfully scanned animals that were returned to food developed normally into adults without gross morphological defects.

Unfixed Tissue Imaging of Adult Retina: Adult animals younger than 5 days old were sacrificed and mounted at the center of a petri dish (10 × 35 mm, Thermo Scientific) using nail-polish (Amazon) with cold distilled water. Samples were positioned such that the targeted eye region (dorsal-posterior or ventral-anterior regions) was placed on the flat surface. Imaging was performed using an Olympus two-photon microscope with 920 nm excitation and an Olympus 25x water-immersion objective. Images compromised by air-bubble entrapment, preventing clear visualization, were excluded from analysis.

Confocal Imaging of Fixed Tissue: Fixed samples were imaged using a Leica SP8 confocal microscope or a Leica Stellaris confocal microscope with STED module (**Figure 4A**) with a 63x glycerol-immersion objective lens. Samples were positioned such that the targeted eye region (dorsal-posterior or ventral-anterior regions) was placed on the flat surface. Images were analyzed using FIJI (ImageJ) and Imaris for further analysis.

Cryosection: Adult or pupal heads were fixed, processed through a sucrose gradient, embedded in OCT, cryosectioned at 12 µm, and postfixed. We focused exclusively on the dorsal-posterior region, as its proximity to the flat center of the adult eye allows more robust sectioning (**Figure 6D1-5**). Detailed protocols are provided in supplementary references (*85*).

Immunohistochemistry: Fly pupal retina and optic lobes were dissected, fixed, blocked, and stained using standard immunohistochemistry protocols. Full details are provided in supplementary references (*86*).
The following primary antibodies were used for immunofluorescence: mouse anti-Dlg1 (1:200, 4F3, DSHB), rabbit anti-HA (1:200, Cell Signaling Technologies), rat anti-FLAG (1:200, Novus), mouse Anti-V5-tag:DyLight550 (1:200, BioRad), guinea pig anti-inx1 (1:1k, GenScript), rabbit anti-inx2 (1:2k, M. Hoch), guinea pig anti-inx3 (1:1k, GenScript), rabbit anti-inx4 (1:1k, A. Borst), rabbit anti-inx5 (1:1k, A. Borst), rabbit anti-inx6 (1:1k, A. Borst), rabbit anti-inx7 (1:1k, A. Borst), rabbit anti-inx8 (1:1k, A. Borst), chicken anti-GFP (1:1k, EMD), rat anti-Ecad (1:10, DSHB, DCAD2), AlexaFluor660 conjugated Phalloidin (Invitrogen, 1:200), and AlexaFluor405 conjugated Goat Anti-HRP (Jackson ImmunoResearch, 1:100). Secondary antibodies were from Invitrogen and used at 1:200.

TrpA Heat Activation: Pupae at 37hAPF were selected, attached to double-sided taped glass slides, and the pupal case around the retinas was removed. Animals were then incubated in a dark 29°C incubator for the designated time, followed by transfer to a 25°C incubator with wet Kimwipes to maintain humidity. Samples were dissected at 46hAPF (**Figure 5**), 72hAPF (**Figure 6A**), and the adult stage (**Figure 6D**) for further analysis. Animals showing obvious

signs of cellular toxicity from heat induction, such as darker pigmentation or scarring, were excluded from experiments.

QUANTIFICATION AND STATISTICAL ANALYSIS

Quantification of Retinal Wave-Induced Calcium Activity: Calcium imaging data from SP8 confocal microscopy of whole retinas was quantified using a hybrid model integrating event detection and intensity measurement for improved sensitivity and accuracy. Time-lapse images were pre-processed in Fiji to obtain corrected F/F0 values. ROIs for individual ommatidia were defined in a semi-automatic manner for further analysis in R. A two-component Gaussian mixture model (GMM) was applied to classify each ROI in each frame as "On" or "Off", with thresholds semi-manually optimized to enhance detection accuracy. Total calcium activity was calculated by summing ΔF/F0 values exclusively during "On" states, reducing background noise and ensuring meaningful activity quantification. This approach improves sensitivity and accuracy by combining event frequency and intensity.

Calcium imaging data from two-photon microscopy with limited ROIs at single-cell resolution was quantified by integrating all ΔF/F0 intensity values to capture total calcium signal magnitude. Time-lapse images were pre-processed in Fiji to obtain corrected F/F0 values. All ΔF/F0 values across corresponding frames were summed to quantify total calcium activity. ROIs for individual cell types were defined semi-automatically. Retinal pathways were manually defined, considering sequential activation of calcium activity from adjacent cells.

Quantification of Regional Ommatidial Morphology:

For whole-retina-level ommatidial size distribution, retinas expressing longGMR-GAL4-driven membrane-tethered GFP were imaged in intact animals using a two-photon microscope with 0.3 μm voxel size. The entire retina was scanned to reconstruct a 3D retinal surface, and individual ommatidial hexagonal areas were calculated using Imaris software, which semi-automatically detected the apical side of each hexagonal corner point. For finer size and ommatidial boundary measurements, dissected retinas immunostained with Dlg1 were mounted to position the region of interest on a flat area. Images were acquired using an SP8 confocal microscope and analyzed with Imaris software for more detailed definitions of interommatidial boundaries. Along a hypothetical line connecting two ommatidial centers, the distance between the most apical points of interommatidial Dlg1 staining was measured as the interommatidial gap size. Among the six interommatidial gaps within a single ommatidium, the two gaps along the DV axis where 1PC/1PC meet were excluded due to their consistently smaller apical domain of 2P. The average of the other four gaps was assigned for each ommatidium.

Other Quantifications

Innexin Intensity (Supplementary Figure 4G-I): Fixed pupal retinas were stained with innexin antibodies and Dlg1. Images were acquired using an SP8 confocal microscope, and innexin intensity within interommatidial junctional Dlg1 was quantified.

Coefficient of Variation of Sqh-GFP (Figure 5I,K): Retinas expressing Sqh-GFP were imaged in intact animals using a two-photon microscope with a 0.4 μm voxel size to reconstruct the 3D retinal surface. Images were analyzed using Imaris with manual refinement to define ROIs corresponding to the apical interommatidial boundary areas. To quantify local clustering of Sqh-GFP signal, the coefficient of variation (CV) was calculated within these defined ROIs. All pixel intensity values within the ROI were extracted, and the CV was calculated as the ratio of the

standard deviation to the mean intensity of these pixels. Higher CV values indicate greater intensity heterogeneity, reflecting localized clustering or accumulation of fluorescence signal.
Pseudocone Quantification (Figure 6): Adult eye pseudocones were imaged using a two-photon microscope at pseudocone layers for targeted eye region (dorsal-posterior or ventral-anterior regions). Using Imaris, pseudocone areas were semi-automatically defined as empty spaces enclosed by interommatidial boundaries.

Statistical Analysis: Male pupae at the same developmental stage within a 1-hour time window were randomly selected from fly vials for all experiments. Blinded analysis across different genotypes was not performed, as genotypes were distinguishable by the experimenter. All experiments were conducted with at least three biological replicates (retinas from three different animals) per genotype. Statistical significance was determined using one-way ANOVA followed by non-parametric t-test. All T-tests and linear regression analyses were performed using GraphPad Prism. Averages and standard deviation/standard error of the mean were calculated using Microsoft Excel.

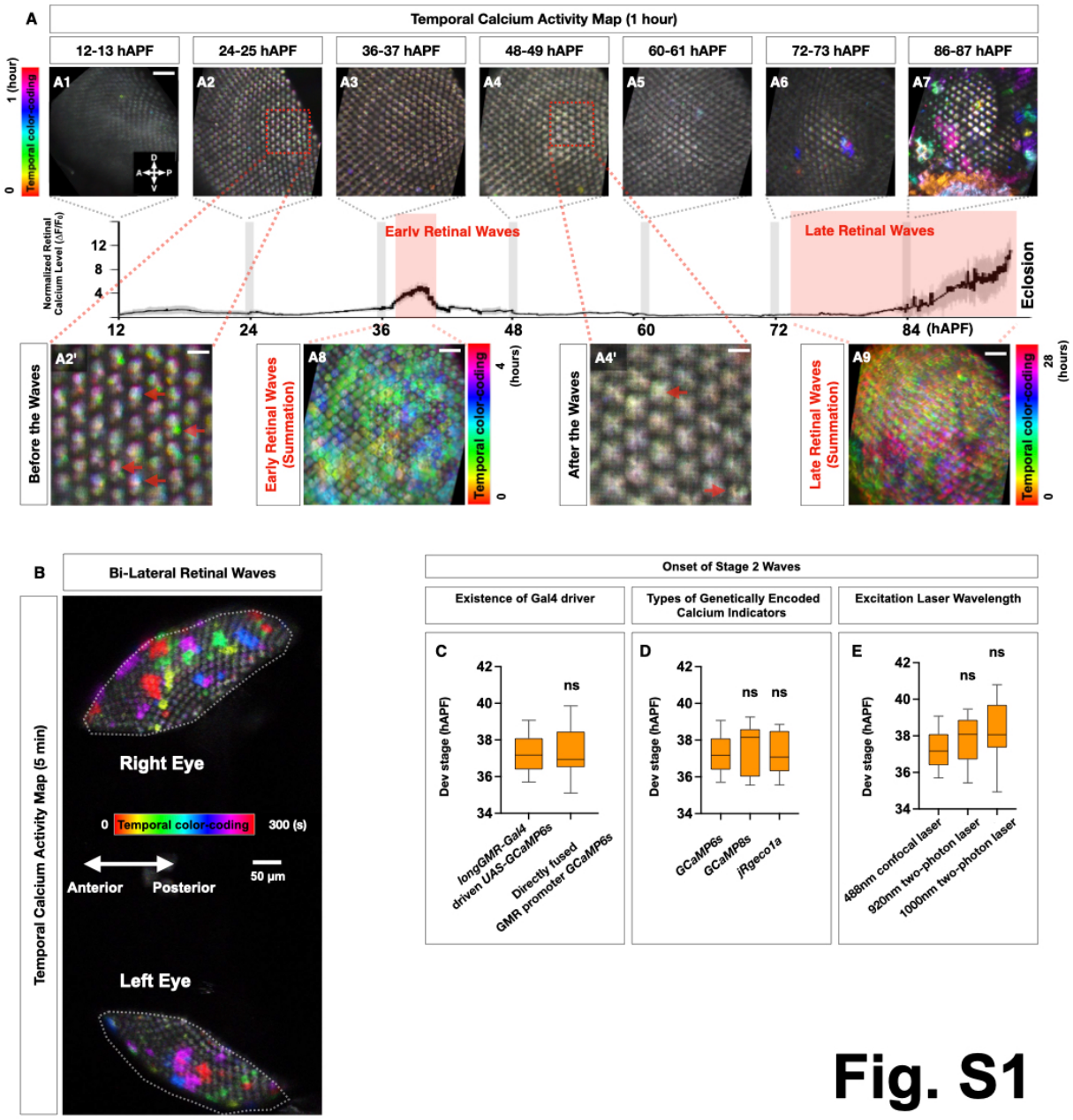
A
Temporal Calcium Activity Map (1 hour)
12-13 hAPF
24-25 hAPF
36-37 hAPF
48-49 hAPF
60-61 hAPF
72-73 hAPF
86-87 hAPF
1 (hour)
Temporal color-coding
0
A1
A2
A3
A4
A5
A6
A7
Normalized Retinal Calcium Level (ΔF/F0)
Early Retinal Waves
Late Retinal Waves
Eclosion
12
24
36
48
60
72
84 (hAPF)
Before the Waves
A2'
Early Retinal Waves (Summation)
A8
4 (hours)
After the Waves
A4'
Late Retinal Waves (Summation)
A9
28 (hours)
B
Bi-Lateral Retinal Waves
Temporal Calcium Activity Map (5 min)
Right Eye
0 Temporal color-coding 300 (s)
Anterior
Posterior
50 µm
Left Eye
Onset of Stage 2 Waves
Existence of Gal4 driver
Types of Genetically Encoded Calcium Indicators
Excitation Laser Wavelength
C
D
E
Dev stage (hAPF)
ns
longGMR-Gal4 driven UAS-GCaMP6s
Directly fused GMR promoter GCaMP6s
GCaMP6s
GCaMP8s
jRgeco1a
488nm confocal laser
920nm two-photon laser
1000nm two-photon laser

Fig. S1

Fig. S1 (A–E) related to Fig. 1.
S1A. Trace of average retinal calcium dynamics throughout pupal retinal development (same as **1B**) with a representative color-coded temporal calcium activity map (1 hour) for each developmental time window (marked in gray window in the trace). **A1–7** show temporal calcium activity maps at every 12-hour interval, with insets of **A2, A4** shown in **A2', A4'** at higher magnification. **A8, A9** display the temporal activity maps for the entire early and late retinal wave periods, respectively. Calcium imaging was performed using *longGMR-GAL4* driving *UAS-GCaMP6s* and images taken at 2-minute intervals, with $n \geq 5$ retinas analyzed per 12-hour time window. Scale bar: 10 µm **(A1–9),** 2.5 µm **(A2', A4').** See also Supplementary **Movie S1**.
S1B. Representative temporal calcium activity map across 5 minutes, covering both eyes during stage 2 retinal waves, demonstrating bilateral wave synchronization. See also Supplementary **Movie S3**.
S1C–E. Quantification of the onset of Stage 2 retinal waves under different experimental conditions. $n \geq 8$ retinas. Calcium imaging was performed using *longGMR-GAL4* driving UAS-transgenes of indicated calcium sensors **(D)** or *UAS-GCaMP6s* **(E)**. ns: $p \geq 0.05$, error bars represent SD.

Fig. S2

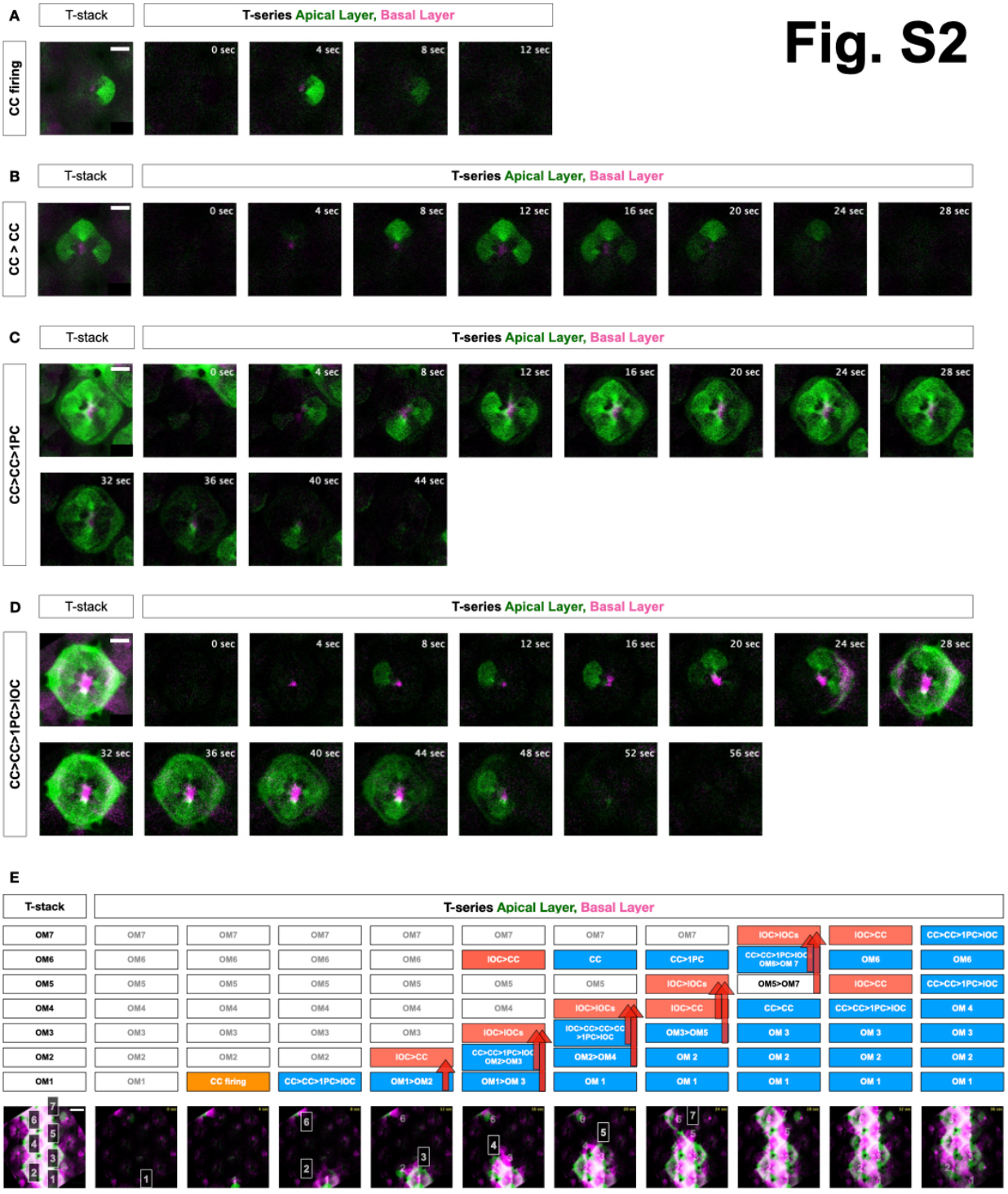
A
T-stack
T-series Apical Layer, Basal Layer
CC firing
0 sec
4 sec
8 sec
12 sec
B
T-stack
T-series Apical Layer, Basal Layer
CC > CC
0 sec
4 sec
8 sec
12 sec
16 sec
20 sec
24 sec
28 sec
C
T-stack
T-series Apical Layer, Basal Layer
CC>CC>1PC
0 sec
4 sec
8 sec
12 sec
16 sec
20 sec
24 sec
28 sec
32 sec
36 sec
40 sec
44 sec
D
T-stack
T-series Apical Layer, Basal Layer
CC>CC>1PC>IOC
0 sec
4 sec
8 sec
12 sec
16 sec
20 sec
24 sec
28 sec
32 sec
36 sec
40 sec
44 sec
48 sec
52 sec
56 sec
E
T-stack
T-series Apical Layer, Basal Layer
OM7
OM6
OM5
OM4
OM3
OM2
OM1
CC firing
CC>CC>1PC>IOC
IOC>CC
IOC>IOCs
CC
CC>1PC
CC>CC>1PC>IOC
OM6>OM 7
OM5>OM7
IOC>CC>CC>CC
>1PC>IOC
OM2>OM3
OM1>OM2
OM1>OM 3
OM2>OM4
OM3>OM5
OM 1
OM 2
OM 3
OM 4

Fig. S2 (A–G) related to Fig. 2.
S2A–D. Representative calcium imaging of the vertical pathway of retinal waves, including single CC firing (**A**), CC to CC (**B**), CC to CC to 1PC (**C**), and CC to CC to 1PC to IOC (**D**). Integrative T-stacks and individual images of corresponding T-series (4 sec interval) are shown with color-coded layer-specific calcium signal as apical and basal layers in green and magenta, respectively. The apical layer signals mostly originate from CCs and 1PCs, while the basal layer signals mostly originate from IOCs. CC = cone cell, 1PC = primary pigment cell, IOC = inter-ommatidial cells. Scale bar: 5 μm **(A–D).** See also Supplementary **Movie S5**.
S2E. Representative retinal wave propagating across multiple ommatidia using both vertical and lateral pathways. Each box marks marked ommatidia (**OM1–7**) along the wave path where each wave-induced event is color-coded. Yellow indicates spontaneously emerging CC firing, blue indicates vertical propagation within those ommatidia, and red indicates target ommatidia activated by lateral pathways. The red arrow highlights a lateral pathway between two ommatidia. In the frame of 16 sec, OM6 is activated by other waves from outside the imaging area via the lateral pathway. Scale bar: 10 μm**.** See also Supplementary **Movie S6**.

Fig. S3

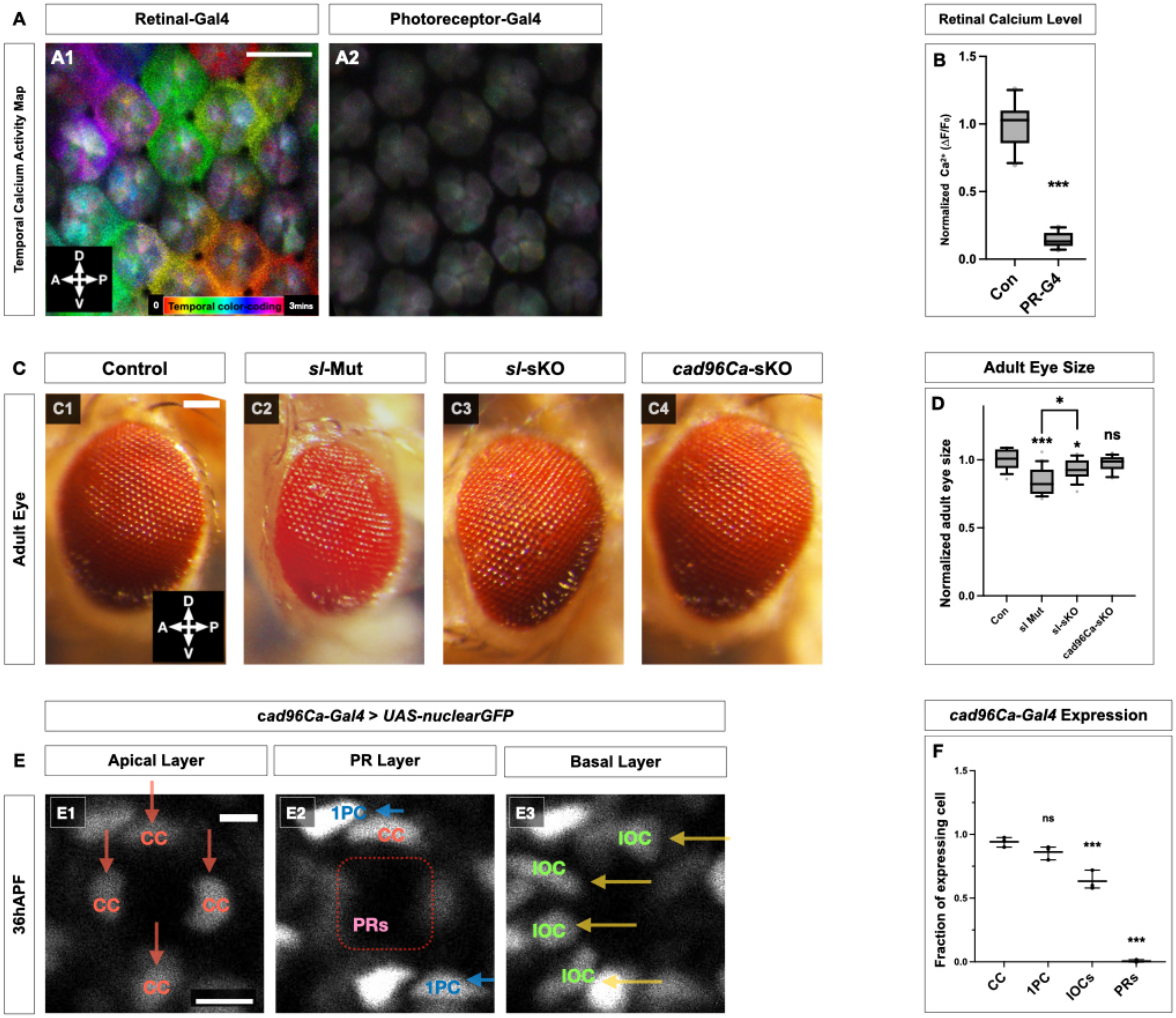
A
Retinal-Gal4
Photoreceptor-Gal4
Temporal Calcium Activity Map
A1
A2
D
A
P
V
0
Temporal color-coding
3mins
Retinal Calcium Level
B
Normalized Ca2+ (ΔF/F0)
1.5
1.0
0.5
0.0
***
Con
PR-G4
C
Control
sl-Mut
sl-sKO
cad96Ca-sKO
Adult Eye
C1
C2
C3
C4
Adult Eye Size
D
Normalized adult eye size
*
***
*
ns
Con
sl Mut
sl-sKO
cad96Ca-sKO
cad96Ca-Gal4 > UAS-nuclearGFP
E
Apical Layer
PR Layer
Basal Layer
36hAPF
E1
E2
E3
CC
1PC
PRs
IOC
cad96Ca-Gal4 Expression
F
Fraction of expressing cell
ns
***
***
CC
1PC
IOCs
PRs

Fig. S3 (A–F) related to Fig.s 2 and 3.
S3A. Representative images of retinal wave activity, displayed as color-coded 3-minute temporal calcium activity maps from pan-retinal GAL4 (longGMR-GAL4) **(A1)** and a photoreceptor-specific GAL4 (Chaoptin-GAL4) **(A2)** retinas during stage 2 (**A1**) or corresponding time window (**A2**). **A2** shows no meaningful calcium activity. Scale bar: 10 µm **(A1, A2).** See also Supplementary **Movie S7**.
S3B. Quantification of the level of retinal calcium signal from **S3A**. $n \geq 8$ retinas, *** : $p < 0.001$, error bars represent SD.
S3C. Representative images of adult eyes from control **(C1),** *sl* null mutant **(C2),** *sl*-sKO **(C3),** and *cad96Ca*-sKO **(C4).**
S3D. Quantification of adult eye size from **S3C.** $n \geq 14$ retinas, ns ≥ 0.05, *: $p < 0.05$, ***: $p < 0.001$. Error bars represent SD.
S3E. Live imaging snapshots of retinas at 36hAPF, using a nuclear GFP reporter driven by *cad96Ca-GAL4*. Each panel represents a single Z-section of retinal layers from apical **(E1),** photoreceptor **(E2),** and basal **(E3)** layers. CC = cone cell, PR = photoreceptor, 1PC = primary pigment cell, IOC = interommatidial cell.
S3F. Quantification of the fraction of *cad96Ca-GAL4* expressing cell-types from **S3E.** **$n \geq 93$ cells from 3 retinas, ns ≥ 0.05, ***: $p < 0.001$.

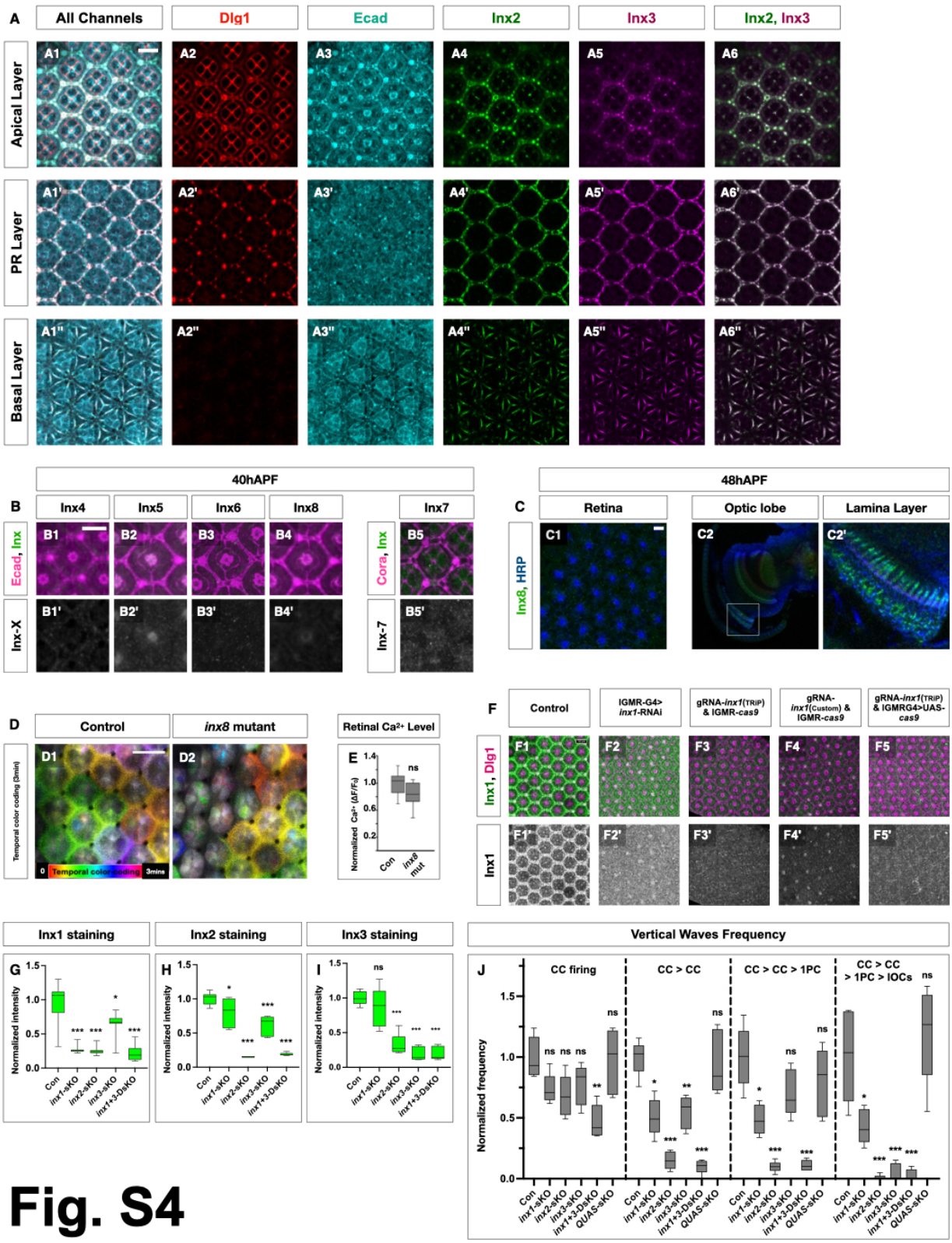
A
All Channels
Dlg1
Ecad
Inx2
Inx3
Inx2, Inx3
Apical Layer
PR Layer
Basal Layer
B
40hAPF
Inx4
Inx5
Inx6
Inx8
Inx7
Ecad, Inx
Cora, Inx
Inx-X
Inx-7
C
48hAPF
Retina
Optic lobe
Lamina Layer
Inx8, HRP
D
Control
inx8 mutant
Temporal color coding (3min)
Temporal color coding
Retinal Ca2+ Level
Normalized Ca2+ (ΔF/F0)
Con
inx8 mut
F
Control
IGMR-G4> inx1-RNAi
gRNA-inx1(TRIP) & IGMR-cas9
gRNA-inx1(Custom) & IGMR-cas9
gRNA-inx1(TRIP) & IGMRG4>UAS-cas9
Inx1, Dlg1
Inx1
Inx1 staining
Inx2 staining
Inx3 staining
Normalized intensity
Con
Inx1-sKO
Inx2-sKO
Inx3-sKO
Inx1+3-DsKO
Vertical Waves Frequency
CC firing
CC > CC
CC > CC > 1PC
CC > CC > 1PC > IOCs
Normalized frequency
QUAS-sKO

Fig. S4

Fig. S4 (A–J) related to Fig. 4.

S4A. Representative immunostaining images of Inx2 and Inx3 in 40hAPF retinas. These Z-stack images display the apical layer **(A1–A6)**, photoreceptor (PR) layer **(A1'–A6')**, and basal layer **(A1''–A6'')**. Gap junction plaques containing Inx2 and Inx3 are observed at retinal support cell junctions, labeled with either Dlg1 (red) or E-cadherin (cyan). No Inx2 or Inx3 plaques were detected around PR cell bodies, indicated by empty space in the center of the ommatidium **(A6')**, confirming that gap junctions are primarily in retinal non-neuronal cells. Scale bar: 10 µm **(A1-6).**

S4B. Representative immunostaining images of Inx4–8 (Inx-X) in 40hAPF retinas, with innexins **(white for B1'–5')** and adherens junctional marker E-cadherin **(magenta for B1–4)** or septate junctional marker Coracle **(B5)**. No significant Inx 4–8 signals were detected at ommatidial junctions at 40hAPF retina, with weak Inx5 signal from the early rhabdomere **(B2)**. Scale bar: 10 µm **(B1-5).**

S4C. Immunostaining of Inx8 in retinas **(C1)** and photoreceptor axonal terminals **(C2, C2')** at 48hAPF, using Inx8 **(**green**)** and neuronal membrane marker HRP **(**blue**)**, respectively. No meaningful signal was detected in the retina **(C1)**, suggesting the subcellular localization of Inx8 in PRs is confined to axonal terminals located in the optic lobe **(C2)**. Scale bar: 10 µm **(C1,2).**

S4D. Representative images of retinal wave activity, displayed as color-coded 3-minute temporal calcium activity maps from control **(D1)** and *inx8* mutant retinas **(D2)** during stage 2 waves. Scale bar: 10 µm **(D1,2).** See also Supplementary **Movie S11**.

S4E. Quantification of retinal calcium levels from **S4D.** $n \geq 6$ retinas, ns: $p \geq 0.5$. Error bars represent SD.

S4F. Representative retinal images of transgenic *inx1* mutants at 40hAPF, including control **(F1, F1'),** *inx1-RNAi* **(F2, F2'),** *gRNA-inx1* (BDSC version) with *longGMR-Cas9* **(F3, F3'),** *gRNA-inx1* (custom version) with *longGMR-Cas9* (referred as ***inx1*-sKO**) **(F4, F4'),** and *gRNA-inx1* (BDSC version) with *longGMR-G4 > UAS-Cas9* **(F5, F5')**, using Inx1 **(green)** and junctional marker Dlg1 **(**magenta**)**, respectively. The images are Z-stacks of the retinal apical layer. Scale bar: 10 µm **(F1-5).**

S4G–I. Quantification of Inx1 **(G),** Inx2 **(H),** and Inx3 **(I)** immunostaining signals in *inx*s-sKO mutant retinas from **Fig. 4B**. $n \geq 14$ retinas, ns: $0.5 \geq p$, *: $p < 0.5$, **: $p < 0.01$, ***: $p < 0.001$. Error bars represent SD.

S4J. Quantification of vertical pathway frequency for each step indicated above in *inx* mutant retinas during late stage 1. All values were normalized to control. $n \geq 200$ ommatidia from 5 retinas, ns: $0.5 \geq p$, *: $p < 0.5$, **: $p < 0.01$, ***: $p < 0.001$. Error bars represent SD.

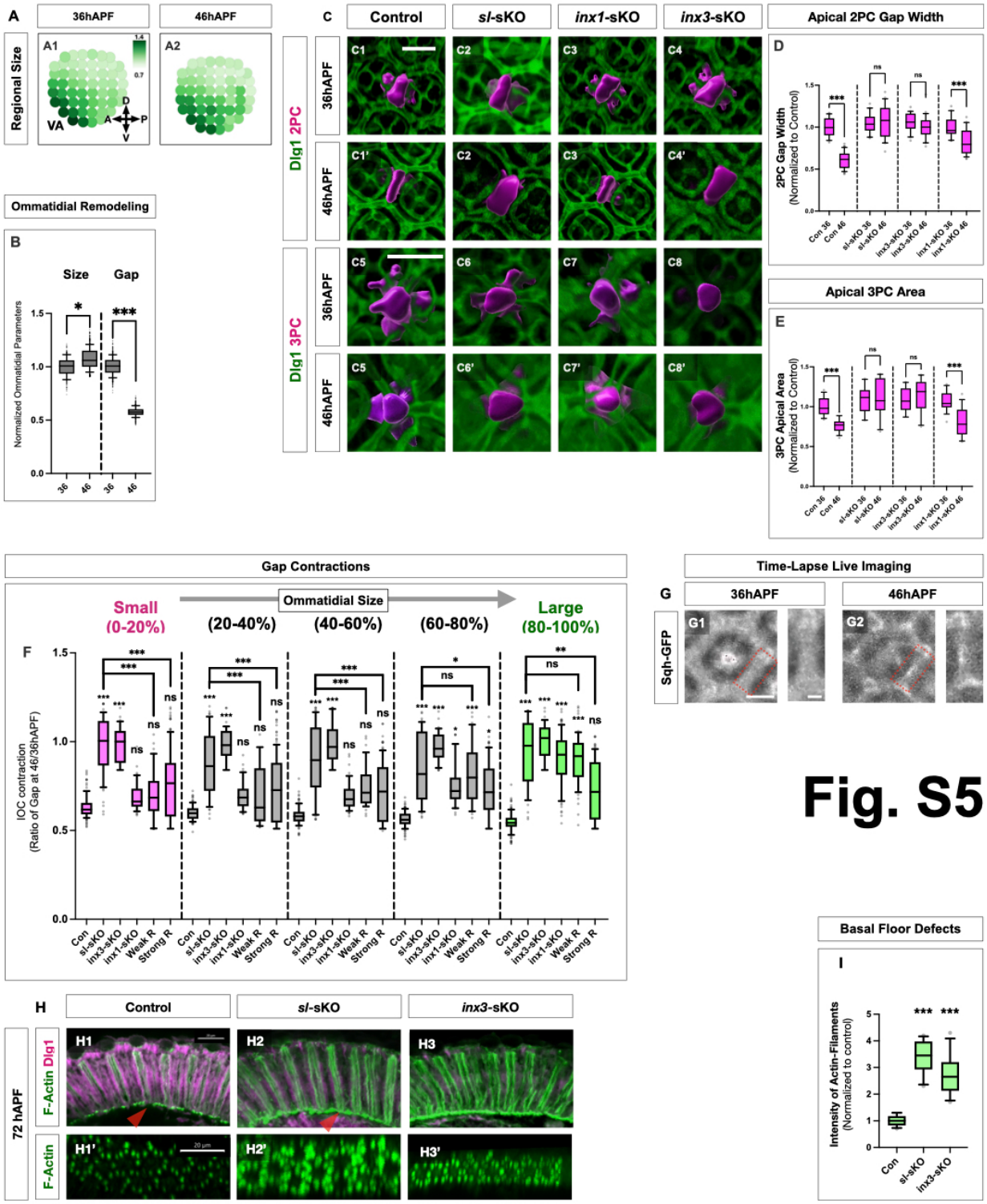
A
36hAPF
46hAPF
Regional Size
A1
A2
VA
D
A
P
V
Ommatidial Remodeling
B
Size
Gap
Normalized Ommatidial Parameters
C
Control
sl-sKO
inx1-sKO
inx3-sKO
Dlg1 2PC
Dlg1 3PC
36hAPF
46hAPF
Apical 2PC Gap Width
D
2PC Gap Width (Normalized to Control)
Apical 3PC Area
E
3PC Apical Area (Normalized to Control)
Gap Contractions
Ommatidial Size
Small (0-20%)
(20-40%)
(40-60%)
(60-80%)
Large (80-100%)
F
IOC contraction (Ratio of Gap at 46/36hAPF)
Con
sl-sKO
inx3-sKO
inx1-sKO
Weak R
Strong R
Time-Lapse Live Imaging
G
Sqh-GFP
G1
G2
H
72 hAPF
F-Actin Dlg1
F-Actin
H1
H2
H3
H1'
H2'
H3'
Basal Floor Defects
I
Intensity of Actin-Filaments (Normalized to control)

Fig. S5

Fig. S5 (A–I) related to Fig. 5.
S5A. Population data using an 8×8 grid to display ommatidial size distribution **(A1, A2)** for control at 36hAPF **(A1)** and 46hAPF **(A2).**
S5B. Quantification of individual ommatidial size and inter-ommatidial gaps between 36hAPF (blue) and 46hAPF (red) from ommatidia labeled with Dlg1 **(Fig. 5C).** Definition of each parameter is shown in **Fig. 5D.** $n \geq 389$ ommatidia from $n \geq 9$ retinas, *: $p < 0.05$, ***:** $p < 0.001$**.** Error bars represent SD.
S5C. Representative 3D-reconstructed images of secondary and tertiary pigment cells (2PCs, 3PCs) at different stages **(36hAPF: C1–8; 46hAPF: C1'–8')** in different genetic backgrounds, labeled with membrane-tethered MCFO-epitope tag (magenta) and Dlg1 (green). Scale bar: 10 µm **(C1-8, C1'-8').**
S5D, E. Quantification of apical contraction of gap-width in 2PCs as related to control size **(E)** and 3PC area **(F).** $n \geq 32$ 2PCs, $n \geq 18$ 3PCs from ≥10 retinas per genotype, *: $p < 0.05$, **: $p < 0.01$, ***:** $p < 0.001$**.** Error bars represent SD.
S5F. Quantification of inter-ommatidial gap contraction with various sizes of ommatidia using Dlg1 immunostaining **(5C).** The Y-axis represents IOC contraction, calculated as the ratio of 46hAPF inter-ommatidial gap size to that of 36hAPF for each group. $n \geq 105$ ommatidia from $n \geq 16$ retinas per size group, ns : $p \geq 0.05$, *: $p < 0.05$, **: $p < 0.01$, ***: $p < 0.001$. Error bars represent SD.
S5G. Time-lapse images of a single ommatidium at 36hAPF and 46hAPF in the control retina, showing Sqh-GFP puncta in the apical side of inter-ommatidial junction. The red box and side insets highlight apical interommatidial junctions with Sqh-GFP clusters, indicating actomyosin network formation during retinal waves.
S5H. Confocal Z-stack images of horizontal cryosections from 72hAPF retinas, stained with phalloidin (green) for actin filaments and Dlg1 (magenta) for cellular junctions. Side views **(H1–3)** and basal floor views **(H1'–3')** are shown. Red arrowheads indicate abnormal actin filaments at the retinal basal floor. All images were taken with a 10 µm Z-stack thickness.
S5I. Quantification of basal F-actin defects from **S5H.** The X-axis represents genotypes, and the Y-axis shows phalloidin intensity, reflecting actin-filament levels. $n \geq 10$ sections, 4 retinas per genotypes**.** ns : $p \geq 0.05$, *: $p < 0.05$, **: $p < 0.01$, ***: $p < 0.001$. Error bars represent SD.

Table. S1

Gene Symbol	Gene Name	FlyBase ID	Mammalian Homolog	Genetic Manipulation	Gross Retinal Morphology	Early Retinal Waves
alk	**Anaplastic lymphoma kinase**	FBgn0040505	ALK	UAS-Dominant negative (BL#92968)	normal	normal
cad96Ca	**Cad96Ca/Stitcher**	FBgn0022800	Not known	**guide RNA** (Customized version)	normal	Severe disruption
				UAS-RNAi (BL#55877)	normal	Mild disruption
ddr	**Discoidin domain receptor**	FBgn0053531	DDR1 and DDR2	UAS-RNAi (BL#55906)	normal	normal
dnt	**Doughnut on 2**	FBgn0024245	RYK	**guide RNA** (Customized version)	normal	normal
				UAS-RNAi (BL#67251)	normal	normal
drl	**Derailed**	FBgn0015380	RYK	**guide RNA** (Customized version)	normal	normal
				UAS-RNAi (BL#39002)	normal	normal
egfr	**breathless**	FBgn0003731	EGFR	UAS-Dominant negative (BL#5364)	Severe disruption	Mild disruption
eph	**Eph receptor tyrosine kinase**	FBgn0025936	EPHA and EPHB	**guide RNA** (Customized version)	normal	normal
				UAS-RNAi (BL#60006)	normal	normal
inR	**Insulin-like receptor**	FBgn0013984	INSR/IGF1R	UAS-Dominant negative (BL#8253)	normal	normal
nrk	**Neurospecific receptor kinase**	FBgn0020391	MuSK	UAS-RNAi (BL#56936)	normal	normal
otk	**off-track**	FBgn0004839	Wnt4	**guide RNA** (Customized version)	normal	normal
pvr	**PDGF- and VEGF-receptor related**	FBgn0032006	VEGFR and PDGFR	**guide RNA** (Customized version)	Mild disruption	Mild disruption
				UAS-Dominant negative (BL#58431)	Mild disruption	Mild disruption
ret	**Ret oncogene**	FBgn0011829	RET	UAS-RNAi (BL#55872)	normal	normal
sev	**sevenless**	FBgn0003366	Not known	UAS-RNAi (BL#55866)	normal	normal
tie	**Tie-like receptor tyrosine kinase**	FBgn0014073	Not known	**guide RNA** (Customized version)	normal	normal
tor	**torso**	FBgn0003733	Not known	**guide RNA** (Customized version)	normal	Mild disruption
				UAS-RNAi (BL#58312)	normal	normal
Control	**QUAS sequence**			**guide RNA** (Customized version)	normal	normal

Supplementary Movie Legends

Movie S1. Calcium dynamics of developing pupal retina from 12hAPF to eclosion (A–I), related to **Fig. S1A.** Representative calcium imaging of intact pupal retinas from 12–24hAPF **(A),** 24–36hAPF **(B),** 36–48hAPF **(C),** 48–59hAPF **(D),** 60–72hAPF **(E),** 72–84hAPF **(F),** 84hAPF to eclosion **(G),** early retinal waves **(H),** and late retinal waves **(I)** using *UAS-GCaMP6s* driven by *GMR-GAL4* **(A)** or *longGMR-GAL4* **(B–I).** Imaging performed with confocal microscopy (488nm excitation), focusing on retina (**A-G**) or entire pupa (**H, I**). Original GMR-GAL4 is expressed in all retinal cells post-morphogenetic furrow, while longGMR-GAL4 is photoreceptor-specific during the L3 larval eye disc but becomes pan-retinal by 24hAPF. Time-lapse imaging was acquired as Z-stacks at 2 min intervals. Imaging duration was limited to a maximum of 12 hours per pupa to minimize phototoxicity for any analysis.

Movie S2. Retinal calcium waves of a single retina (A–D), related to **Fig. 1C.** Representative retinal calcium wave recordings from a single retina of an intact pupa during early stage 1 **(A),** late stage 1 **(B),** stage 2 **(C),** and stage 3 **(D)** using *UAS-GCaMP6s* driven by *longGMR-GAL4*. Stages are defined in **Fig. 1D.** Imaging performed with confocal microscopy (488nm excitation). Time-lapse imaging was acquired as Z-stacks at 3 sec intervals.

Movie S3. Bilateral retinal calcium waves, related to **Fig. S1C.** Representative recording of bilateral retinal calcium waves from both eyes of a single animal during retinal waves using *UAS-GCaMP6s* driven by *longGMR-GAL4.* Imaging performed with confocal microscopy (488nm excitation). Time-lapse imaging was acquired as Z-stacks at 2 minutes intervals.

Movie S4. Retinal calcium waves at single-cell resolution (A–D), related to **Fig. 2C.** Representative recordings of retinal calcium waves from a single retina during early stage 1 **(A),** late stage 1 **(B),** stage 2 **(C),** and stage 3 **(D)** using *UAS-GCaMP6s* driven by *longGMR-GAL4.* Imaging performed with two-photon microscopy (920nm excitation). Time-lapse imaging was acquired as Z-stacks at 5 sec intervals.

Movie S5. Vertical pathways of retinal calcium waves (A–D), related to **Fig. S2A–D.** Representative recordings of retinal calcium waves during stage 1 showing initial cone cell firing **(A),** cone cell to cone cell signaling **(B),** cone cell to cone cell to primary pigment cell signaling **(C),** and cone cell to cone cell to primary pigment cell to interommatidial cells **(D).** Imaging performed with two-photon microscopy (920nm excitation). Z-stacks were acquired every 4 sec. Apical and basal layers are color-coded as green (apical) and magenta (basal).

Movie S6. Lateral pathways of retinal calcium waves, related to **Fig. S2E.** Representative recordings of retinal calcium wave propagation across multiple ommatidia during stage 2 using *UAS-GCaMP6s* driven by *longGMR-GAL4.* Imaging performed with two-photon microscopy (920nm excitation). Z-stacks were acquired every 4 sec. Apical and basal layers are color-coded as green (apical) and magenta (basal).

Movie S7. Calcium imaging of photoreceptor neurons during retinal waves, related to **Fig. S3A2.** Representative recording of retinal calcium waves using *UAS-GCaMP6s* driven by

Chaoptin-GAL4 during stage 2. Imaging performed with two-photon microscopy (920nm excitation). Z-stacks were acquired every 4 sec.

Movie S8. Dual-color calcium imaging of ER-released calcium activity during retinal waves (A-C), related to **Fig. 3A.** Representative recording of retinal calcium waves during stage 2 using *UAS-ER-GCaMP6* and *UAS-jRgeco1a* driven by *longGMR-GAL4*. Imaging performed with confocal microscopy (488nm and 561nm excitation). Time-lapse imaging was acquired as Z-stacks at 1 sec intervals. Dual-color imaging with ER-targeted GCaMP (green) and cytosolic jRgeco1a (red) (**A**), ER-targeted GCaMP alone (**B**), and cytosolic jRgeco1a alone (**C**).

Movie S9. Calcium imaging of IP_3R clonal retinas during retinal waves, related to **Fig. 3C2.** Representative recording of retinal calcium waves using *UAS-GCaMP8s* driven *by longGMR-GAL4* in *IP_3R* clonal retinas during stage 2. Imaging performed with two-photon microscopy (920nm excitation). Time-lapse imaging was acquired as Z-stacks at 5 sec intervals.

Movie S10. Calcium imaging of mutants affecting wave initiation (A–E), related to **Fig. 3E.** Representative recordings of retinal calcium waves using *UAS-GCaMP6s* driven by *longGMR-GAL4* in control **(A),** *norpA* mutants **(B),** *sl* mutants **(C),** *sl*-sKO **(D),** and *cad96Ca*-sKO **(E)** during a 5-minute peak intensity window at stage 2. Imaging performed with two-photon microscopy (920nm excitation). Time-lapse imaging was acquired as Z-stacks at 5 sec intervals.

Movie S11. Calcium imaging of *inx8* mutants during retinal waves, related to **Fig. S4D2.** Representative recording of retinal calcium waves using *UAS-GCaMP6s* driven by *longGMR-GAL4 in inx8* mutant retinas during a 5-minute peak intensity window at stage 2. Imaging performed with two-photon microscopy (920nm excitation). Time-lapse imaging was acquired as Z-stacks at 5 sec intervals.

Movie S12. Calcium imaging of *inx* mutants during retinal waves (A–E), related to **Fig. 4C.** Representative recordings of retinal calcium waves using *UAS-GCaMP6s* driven by *longGMR-GAL4* in control **(A),** *inx1*-sKO **(B),** *inx2*-sKO **(C),** *inx3*-sKO **(D),** and *inx1+3*-DsKO **(E)** during a 5-minute peak intensity window at stage 2**.** Imaging performed with two-photon microscopy (920nm excitation). Time-lapse imaging was acquired as Z-stacks at 5 sec intervals.

Supplementary references

85. N. Ghosh, J. E. Treisman, Apical cell expansion maintained by Dusky-like establishes a scaffold for corneal lens morphogenesis. *Sci Adv* **10**, eado4167 (2024).
86. J. A. Malin, Y. C. Chen, F. Simon, E. Keefer, C. Desplan, Spatial patterning controls neuron numbers in the Drosophila visual system. *Dev Cell* **59**, 1132-1145 e1136 (2024).